The Geological Society of America
Special Paper 531

A new sequence stratigraphic model for the Silurian A-1 Carbonate (Ruff Formation) of the Michigan Basin

Matthew J. Rine
Stephen E. Kaczmarek
Jonathan D. Garrett
Department of Geosciences, Western Michigan University,
1903 W. Michigan Avenue, Kalamazoo, Michigan 49008-5241, USA

ABSTRACT

The A-1 Carbonate is the primary hydrocarbon source rock and an important reservoir component of the Silurian (Niagaran) pinnacle reef complexes in the Michigan Basin. The geology of the A-1 Carbonate, however, is not widely known because the majority of published research about this hydrocarbon system focuses on the pinnacle reefs. To gain a better understanding of the sedimentology and stratigraphy of the A-1 Carbonate, we integrated data from slabbed core, thin section petrography, gamma-ray logs, and energy-dispersive X-ray fluorescence spectrometry (ED-XRF). Thirteen distinct lithofacies within the A-1 Carbonate are recognized, with inferred depositional environments ranging from intertidal-sabkha to deep basin. The recognition of deep-water lithofacies contrasts significantly with previous interpretations of the A-1 Carbonate as a shallow, peritidal deposit.

Lithofacies stacking patterns and ED-XRF elemental trends within the A-1 Carbonate are consistent with basinwide sea-level fluctuations that resulted in deposition of three major stratigraphic units, called the Lower A-1 Carbonate, Rabbit Ear Anhydrite, and Upper A-1 Carbonate. The basal part of the Lower A-1 Carbonate was deposited during a basinwide transgression, as evidenced by deep-water pelagic carbonate accumulation in the basin center, lithofacies that become progressively muddier from bottom to top, and higher concentrations of Si, Al, and K upward, which are interpreted to reflect the influx of continental sediments. The subsequent highstand deposits of the upper part of the Lower A-1 Carbonate are characterized by a decrease in Si, Al, and K, coupled with a shallowing-upward facies succession consistent with increased carbonate production rates. The Rabbit Ear Anhydrite, which bifurcates the Upper and Lower A-1 Carbonate units, exhibits a variety of anhydrite fabrics across a wide range of paleotopographic settings within the basin. The Rabbit Ear Anhydrite is interpreted to reflect a time-correlative sea-level drawdown, which caused basin restriction, gypsum deposition, and elevated concentrations of redox-sensitive elements, such as Mo and Ni. The Upper A-1 Carbonate represents

Rine, M.J., Kaczmarek, S.E., and Garrett, J.D., 2017, A new sequence stratigraphic model for the Silurian A-1 Carbonate (Ruff Formation) of the Michigan Basin, *in* Grammer, G.M., Harrison, W.B., III, and Barnes, D.A., eds., Paleozoic Stratigraphy and Resources of the Michigan Basin: Geological Society of America Special Paper 531, p. 175–195, doi:10.1130/2017.2531(09).

sedimentation during another major basinwide transgression that culminated in the deposition of shallow-water microbialites on the crests of previously exposed Niagara reef complexes. Similar to the Lower A-1 Carbonate, the base of the Upper A-1 Carbonate exhibits elemental signatures indicative of continental influence, whereas the overlying highstand deposits are characterized by more normal marine conditions and lower concentrations of Si, Al, and K.

INTRODUCTION

Economic Importance of the A-1 Carbonate

Despite its reputation as an important depositional unit within the Michigan Basin, only a few studies (e.g., Gill, 1973, 1977; Budros, 1974; Budros and Briggs, 1977) have given careful consideration to the geology of the A-1 Carbonate. Instead, nearly all investigations of the stratigraphy and hydrocarbon potential of Niagara–Lower Salina reef complex reservoirs have focused on the pinnacle reefs (e.g., Alling and Briggs, 1961; Mesolella et al., 1974; Sears and Lucia, 1979; Friedman and Kopaska-Merkel, 1991; Grammer et al., 2009; Rine et al., 2017; Ritter and Grammer, this volume; Wold and Grammer, this volume). The A-1 Carbonate (Ruff Formation) constitutes an important component of overall Niagara–Lower Salina reef-complex reservoirs across the basin. Total organic carbon (TOC) in the A-1 Carbonate has been measured as high as 3%, but is generally ~1% (Obermajer et al., 2000). Elevated TOC levels coupled with its vast areal extent (~16,000 km^2) and significant thickness (15–35 m) led Gardner and Bray (1984) to implicate the A-1 Carbonate as the primary hydrocarbon source rock for the Niagara–Lower Salina reservoirs. Lithofacies distributions and stratigraphic relationships between the A-1 Carbonate and the underlying Brown Niagaran reef deposits of the Guelph Formation (herein referred to as the Niagaran), however, are unknown.

Technological advances triggered by production from unconventional shale reservoirs have recently spurred renewed interest in the A-1 Carbonate as a hydrocarbon target. A Michigan Department of Environmental Quality report (2015) published by the Office of Oil, Gas, and Minerals indicates that hydrocarbon production occurs in 31 A-1 Carbonate fields, where it is either the sole producing unit or produces in combination with the Niagaran reefs. Compared to the ~500 million barrels of oil (MMBO) and ~3 trillion cubic feet (TCF) of natural gas reported for the Niagaran, production statistics indicate that ~3.3 MMBO and 37.5 billion cubic feet (BCF) of gas have been produced directly from the A-1 Carbonate. Michigan Geological Survey well records also indicate that many reports of Niagaran production are from wells that were actually completed in the A-1 Carbonate. In fact, well data from Otsego County show that >30% of total oil production and ~24% of total gas production attributed to the Niagaran actually came from the A-1 Carbonate, with some wells in the A-1 Carbonate producing as much as 1 MMBO (e.g., Chester 6 field). Because production from the A-1 Carbonate is often reported generically as "Niagaran," the overall contribution of the A-1 Carbonate reservoir unit is likely to be vastly underestimated.

In general, recent hydrocarbon production from the A-1 Carbonate has focused on four principal hydrocarbon plays, all of which are concentrated on dolomitized and/or fractured reservoirs. Dolomitized intervals of the A-1 Carbonate often display better reservoir quality than the underlying and adjacent Niagaran reefs. This is especially the case in Niagaran reefs located along the northern trend, where dolomitization, and thus reservoir quality, within the Niagaran component of reef complexes decreases toward the basin center (Sears and Lucia, 1979).

Geologic Setting

The Michigan Basin is a circular, intracratonic basin covering an area of 316,000 km^2 (Catacosinos et al., 1991). During the Niagaran (Middle–Late Silurian), the Michigan Basin was located between 20°S and 25°S in a tropical to subtropical environment experiencing southeasterly to easterly equatorial trade winds (Briggs and Briggs, 1974; Scotese, 2002; Rine et al., 2017; Wold and Grammer, this volume). Basin location provided favorable environmental conditions for carbonate reef growth until the late Niagaran (Wenlockian; Mesolella et al., 1974). The Niagaran reefs developed on a gently sloping shelf that acted as a transitional belt between the stable carbonate platform that rimmed the basin and the deep basin interior (Fig. 1A; Friedman and Kopaska-Merkel, 1991).

A significant regression during the Niagaran resulted in the progressive exposure and demise of Niagaran carbonate banks and pinnacle reefs. This sea-level drawdown is evidenced by widespread deposition of gypsum, halite, and sylvite of the Salina A-1 Evaporite formation (Gill, 1977; Nurmi and Friedman, 1977). Leibold (1992) reported that in the basin center, potash (KCl) salts are underlain by a regressive package of halite and overlain by a transgressive package of halite, with the whole evaporite package totaling as much as 122 m (400 ft). The subsequent transgressive deposits of the A-1 Carbonate conformably onlap the A-1 Evaporite in the basin center (Fig. 1B; Leibold, 1992; Budros and Briggs, 1977) and drape the underlying Niagaran reefs (Mantek, 1973; Gill, 1985; Rine et al., 2017). Budros and Briggs (1977) implicated the underlying paleotopography of the Niagaran carbonate platform and pinnacle reefs as the main control on the distribution of the A-1 Carbonate in the Michigan Basin. Whereas previous studies disagree about the timing

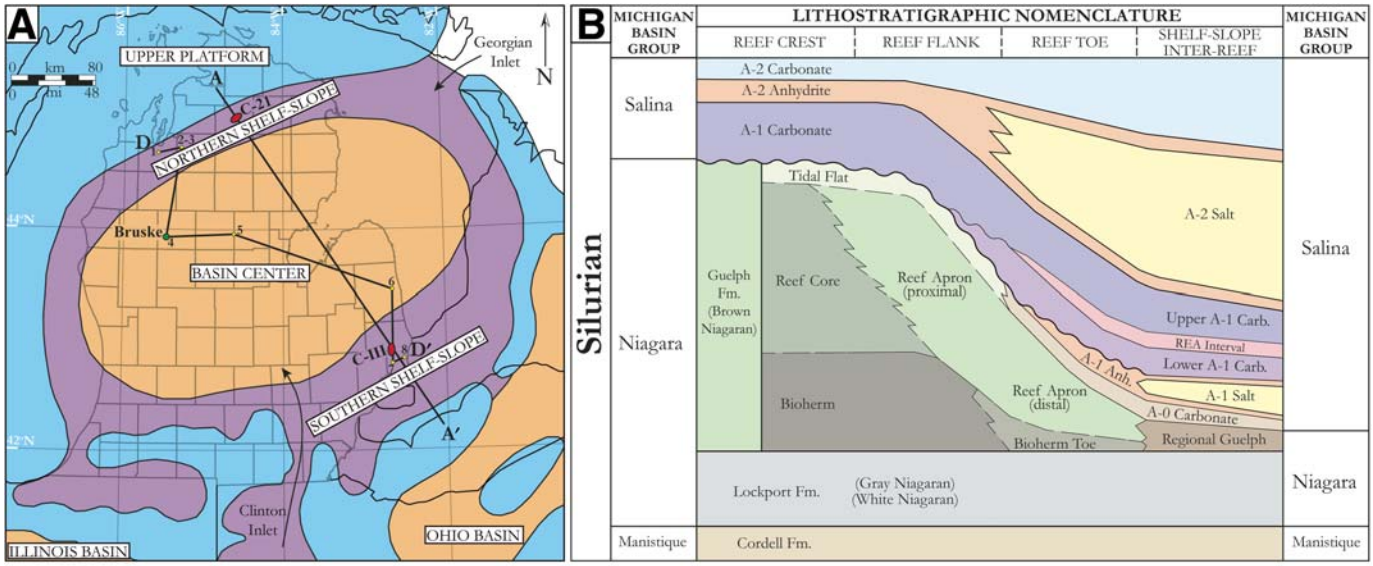

Figure 1. (A) Generalized depositional settings of the Michigan Basin in the Silurian during Niagaran deposition (modified from Briggs et al., 1978). Red ovals mark the locations of the Chester 21 (C-21) and Columbus III (C-III) reef complexes; green circle marks the location of the basin center Bruske well. The A–A′ cross section is represented in Figure 9, and the D–D′ cross section is represented in Figure 10. (B) Lithostratigraphic relations and nomenclature for the Manistique, Niagara, and Lower Salina Groups from the reef crest to shelf-slope inter-reef positions in the Michigan Basin (adapted from Gill, 1985; Rine et al., 2017). REA—Rabbit Ears Anhydrite.

of A-1 Carbonate deposition in the overall Silurian section (see Mesolella et al., 1974), it is widely agreed that the unit is present across the basin and extends over the top of the older Niagaran reefs (e.g., Jodry, 1969; Mantek, 1973; Huh, 1973; Mesolella et al., 1974; Briggs and Briggs, 1974; Sears and Lucia, 1979; Sarg, 1982; Droste and Shaver, 1985; Gill, 1985; Friedman and Kopaska-Merkel, 1991).

Budros and Briggs (1977) described the A-1 Carbonate as an unfossiliferous carbonate mudstone that is variably argillaceous and carbonaceous. These carbonates have been interpreted to represent deposition in shallow subtidal to intertidal settings (Gill, 1973, 1977; Budros, 1974; Budros and Briggs, 1977). The A-1 Carbonate also hosts a series of thin anhydrite beds, referred to as the Rabbit Ear Anhydrite (Fig. 1B). Gill (1973), Huh (1973), and Budros (1974) interpreted these as shallow-water to intertidal sabkha deposits and ephemeral tidal flats located around the periphery of reef complexes. Previous studies by Ells (1967), Budros (1974), and Nurmi (1975) noted the presence of the Rabbit Ear Anhydrite across the basin, but no attempt was made to correlate it.

Here, we present updated facies and sequence stratigraphic models for the A-1 Carbonate in the Michigan Basin. These models are based on integrated data from core description, thin section petrography, gamma-ray logs, and energy-dispersive X-ray fluorescence spectrometry (ED-XRF). The depositional facies model challenges previous interpretations of the A-1 Carbonate as a purely shallow-water deposit, and the sequence stratigraphic model explains the A1-Carbonate in the context of basinwide sea-level changes, restriction, and continental influx.

METHODS

Core Description

Detailed core description was performed on eight slabbed drill cores from three localities within the Michigan Basin (Fig. 1A). Physical attributes recorded included lithology, texture, grain size, sedimentary structures, bed thickness, dip angle, pyritized surfaces, and salt plugging. Six cores were analyzed from the southern shelf slope, five from the northern shelf slope, and one from the basin center. Core names, permit numbers, locations, and data types are reported in Table 1. All four cores

TABLE 1. STUDY WELLS

Field name (basin location)	Permit #	Well name - #	Paleotopographic position	Cored(c) *XRF(x)
Columbus III (S)	27805	Floyd J. Winn B #2	Leeward reef toe	**c-x**
	27851	Floyd J. Winn #2	Leeward reef toe	c
	27539	Floyd J. Winn #1	Leeward reef flank	c
	27572	Harold H. Winn #8	Reef crest	c
Belle River Mills (S)	23797	E. Schunck Unit #1	Leeward reef toe	c
Puttygut (S)	23471	CPC P-102	Reef crest	
N/A (S)	24179	Ruff #1-36	Interreef	c
N/A (BC)	59112	Schultz #1-36	Basin center margin	c
N/A (BC)	59271	Bruske #1-26A	Basin center	**c-x**
N/A (BC)	60451	Wiley #1-18P	Basin center	
Chester 21 (N)	28089	James E. Donovan #1-21	Reef crest	c
	37071	Kenney #4-22A	Windward reef flank	
	28608	Kenney #3-22	Windward reef flank	**c-x**
Kalkaska 21 (N)	28676	Kalkaska #1-22	Reef crest	c
N/A (N)	29218	Kalkaska #2-15	Interreef	c
N/A (N)	27454	Dreves #1	Interreef	c

*Note: XRF: cores analyzed using X-ray fluorescence spectrometry.

in the Columbus III reef complex were located on the western flank of the reef, which is interpreted as the leeward side during Niagaran reef growth, with observed slopes ranging between 15° and 37.5° (Rine et al., 2017). The high-density core coverage in the Columbus III reef complex (32 cores over an area of 2 km^2; ~300 m well spacing) makes it an ideal place to observe lateral facies variations in the A-1 Carbonate.

Observed lithofacies were correlated to gamma-ray (GR) logs to refine formation tops, as well as to identify lithofacies variability where cores were unavailable. Individual core depths were shifted to match log depths. GR signatures and reservoir quality values derived from whole-core permeability measurements are reported in Table 2. Cross sections were constructed for nearly complete A-1 Carbonate intervals in order to develop type section localities for A-1 Carbonate facies. Complete A-1 Carbonate intervals, however, are uncommon in the Michigan Basin wells, especially in the shelf-slope interreef position. Therefore, the utility of core-to-log correlations is to aid in facies and reservoir quality prediction where only wireline log data exist.

ED-XRF Measurements

To further evaluate intra- and interlithofacies variability in texturally homogeneous lithologic units, elemental data were

TABLE 2. A-1 CARBONATE (RUFF FM.) FACIES CLASSIFICATION

Unit	Sketch	Lithofacies	Lithologic attributes	Style of sedimentation	Water depth	Paleo-topographic position	Gamma ray - reservoir quality
Rabbit Ears Anh.		K nodular anhydritic mudstone	Nodular anhydrite textures in a groundmass of micro-laminated carbonate mudstone; white to bluish nodules range from 1 to 5 mm in diameter and are flattened parallel to bedding; interbedded with Facies A and B	Crystal precip. at air-brine interface; pelagic cumulate gypsum "rain"	Shallow subtidal to deep; 3-150 m (restricted)	Basin center; inter-reef; reef toe; reef flank	Med K very low <0.1 mD
		J enterolithic anhydrite	Enterolithic "mosaic" or "chicken-wire" anhydrite textures with large coalescing nodules; bluish nodules range from 1 to 5 cm in diameter; adjacent nodules coalesce, resulting in distorted nodular to enterolithic fabrics	Displacive nodular growth; capillary evaporation below sediment surface	Evaporitic, arid sabkha	Reef crest; reef flank	Med J very low <0.1 mD
		I stromatolitic floatstone	White to tan, angular stromatolitic clasts in a dark greenish-brown, fine-grained, friable, silt matrix; clasts are semi-rounded to angular; associated with high GR values	Erosion of semi-lithified mats & accumulation of wind-blown silt/clay	Subaerial exposure	Reef crest; reef flank	High I medium 1-5 mD
A-1 Carb.		H white crinkly-laminated stromatolitic bindstone	Crinkly-laminated stromatolitic bindstone and associated beds of flat-pebble conglomerate; stromatolites have distinct white to gray color; laminae are thin (mm-scale); associated fragments composed of elongated pebble-size intraclasts	*in situ* benthic microbial trapping & binding	Intertidal; +/- 1 m	Reef crest	Low H medium 1-5 mD
		G laminated agglutinated thrombolitic-stomatolite	Laminated, agglutinated thrombolitic-stromatolite with abundant (mm-scale) peloid grains; peloids are spherical and exist in concentrated beds between wavy, crinkly stromatolitic laminations	*in situ* benthic microbial trapping & binding; crustacean pellet generation	Shallow subtidal; 3-6 m		High G high 5-20 mD
		F thrombolitic bindstone	Thrombolitic bindstone; thrombolites have distinct mottled appearance with dark brown patches of micrite and light tan patches of calcite spar; thrombolite textures vary from ribbon-like to irregular patchy mesoclots	*in situ* benthic microbial trapping & binding			Med F high 10-75 mD
		E stromatolitic rudstone	Clast-supported rudstone composed of elongated, pebble-size, angular, white to tan crinkly-laminated stromatolite intraclasts	High-energy clast rip-up & transport	Intertidal to shallow subtidal; 1-6 m	Reef flank; reef toe; inter-reef; basin center	Slope: med E Basin center: high medium 1-10 mD
		D peloidal packstone	Packstone composed of mm-scale rod-shaped peloids; peloids range from tan (dolomite) to dark brown (limestone) depending on degree of dolomitization; wavy-laminated beds	*in situ* crustacean pellet production		Reef flank	Med D low 0.1-1 mD
		C crystalline dolomite	Crystalline dolomite with occasional swaley laminations; dolomitization is fabric destructive, difficult to identify original depositional fabrics; occasional peloids and carbonaceous mat chips; often associated above/below Facies B	N/A	Diagenetic facies	Reef flank; reef toe	Med C medium 1-5 mD
		B_{iii} laminated peloidal wackestone	Swaley-bedded peloidal wackestone to packstone; abundant mm-scale rod-shaped peloids, often associated with stromatolite clasts; mottled appearance common due to dolomitization of peloids (tan) in lime mud matrix (gray)	Turbidity flows & fine-grain pelagic carbonate sedimentation	Below storm wave base; 20-100 m		Med B_{iii} low 0.1-1 mD
		B_{ii} normally-graded mudstone	Swaley-to-planar bedded mudstone to wackestone; intervals of cm-scale, normally-graded carbonate beds with an abundance of carbonaceous lithoclast chips; lithoclasts consist of peloids, stromatolites, and brachiopod fragments	Turbidity flows & fine-grain pelagic carbonate sedimentation			Med B_{ii} low 0.1-1 mD
		B_i thinly-laminated mudstone	Planar-laminated mudstone similar to Facies A; slightly thicker laminations (cm-scale); often interbedded with Facies A, B_{ii} and B_{iii}	Distal fine-grain pelagic carbonate sedimentation		Reef flank; reef toe; inter-reef; basin center	High B_i low 0.1-1 mD
		A argillaceous carbonate laminite	Planar-laminated carbonate laminite; parting/fissility between thin, mm-scale laminations; laminations characterized by alternating layers of gray micrite with black carbonaceous laminae and quartz silt	Wind blown clay & silt, very distal pelagic carbonate sedimentation	Deep water; 50-150 m	Inter-reef; basin center	High A very low <0.1 mD

collected using an ED-XRF. This technology is widely used in the geosciences, particularly with respect to its ability to resolve stratigraphic shifts in the elemental composition of sediments and rocks (e.g., Haug et al., 2001; Rimmer, 2004; Tjallingii et al., 2007; Algeo and Maynard, 2008; Kujau et al., 2010; Rowe et al., 2012). Elemental data were obtained using a Bruker AXS Tracer IV equipped with a rhodium X-ray tube and silicon-drift detector window.

Elemental data were collected along the slabbed faces of drill cores from the Floyd J. Winn B #2, Kenney #3-22, and Bruske #1-26A wells. To remove salt crusts and other surface contaminants that could potentially cause erroneous results (e.g., Cl routinely causes problems with detecting Mg, Si, and Al), slabs were prepared prior to XRF analysis by dry scrubbing them with a wire brush, blowing them clean with compressed air, and then wet scrubbing them with deionized water and a plastic bristle brush. The core was repeatedly cleaned until Cl and Ba values were reduced to background photon counts or until further washing did not reduce photon counts.

A full suite of XRF elemental data was collected along the length of each core at 15 cm (6 in.) intervals. The X-ray beam analyzes a 3 mm spot, with an analysis depth ranging from 0.096 mm for light elements, such as Mg, to 38 mm for heavy elements, such as Zr. Major element (Mg, Al, Si, P, S, K, Ca, Ti, Mn, Fe) data were collected in low-energy mode for 60 s using a helium flow-through system to purge heavy atmospheric gases, such as argon, from the nose of the instrument where the X-ray source and detector are located. Voltage and current values for major-element analyses were set to 15 kV and 35 μA, respectively. In contrast, trace-element (Ba, V, Cr, Co, Ni, Cu, Zn, As, Ga, Pb, Th, U, Rb, Sr, Y, Sr, Nb, Mo) data were collected for 90 s in high-energy mode with voltage and current values set to 40 kV and 40 μA, respectively. High-energy analyses used an Al-Ti energy filter. Although a full suite of elements was collected during ED-XRF analyses, only a subset is presented composed of the most helpful 10 elements (K, Si, Al, Fe, S, Mo, Ni, Mg, Ca, and Sr). Many of the unreported elements either have concentrations below the instrument detection limit or showed no significant variation throughout the A-1 Carbonate.

Raw photon counts in each XRF spectra were evaluated in Artax, Bruker's proprietary data analysis tool, to detect and correct instrumental artifacts and to ensure that photon peak positions and intensities were correctly identified for each element. Corrected XRF spectra were then imported into S1CalProcess, Bruker's proprietary calibration software, to generate weight percentages for each element. S1CalProcess uses a mathematical transform for each element that is derived using a combination of reference standards from Rowe et al. (2012) and a variety of geological samples from the Michigan Basin. The calibration software essentially cross references XRF photon counts measured by the Tracer IV and elemental concentrations generated from conventional inductively coupled plasma–mass spectrometry (ICP-MS) measurements to correct variable peak heights caused by interelement and baseline shifts (Rowe et al., 2012). This approach is widely utilized by both academia and industry because it allows for the accurate conversion of raw photon counts to elemental weight percentages (Rowe et al., 2012; Pierce and Parker, 2015).

Identification of elemental trends and comparison to core-observed lithofacies was an inherently iterative process. Core observations of certain texturally homogeneous lithologies helped to make sense of unique elemental signatures, and elemental signatures also aided in the visual identification of important compositional changes, such as thin pyritized surfaces. Elemental data proved especially helpful in relatively homogeneous carbonate mudstones because elemental variations helped to identify subtle changes in lithology.

RESULTS

Lithofacies

Sedimentological and geochemical characteristics were used to identify 13 distinct lithofacies in the A-1 Carbonate. Physical descriptions, inferred water depth ranges, sedimentation style, paleotopographic position within the basin, GR signature, and relative permeability of these lithofacies are summarized in Table 2. Representative core photographs are presented in Figure 2. These lithofacies are distributed among three major subunits within the A-1 Carbonate, i.e., the Lower A1-C, the Rabbit Ear Anhydrite, and the Upper A-1 Carbonate.

Paleotopographic Positions

Observed A-1 Carbonate lithofacies occur in five distinct paleotopographic positions within the basin, including: (1) reef crest, (2) reef flank, (3) reef toe, (4) shelf-slope interreef, and (5) basin center (Figs. 3 and 4). Paleotopographic positions are defined by relative location along a depositional dip profile, which is primarily controlled by variations in thickness of the underlying Niagaran strata. These positions provide a consistent and objective means of defining the location of observed lithofacies.

Paleotopographic relief across the Niagaran reef complexes ranges from 3 to 182 m (10–600 ft) as measured from the top of the underlying, mostly flat, Gray Niagaran. Isopach maps of the Brown Niagaran were constructed for the Columbus III and C-21 reef complexes by identifying the tops of the Brown Niagaran and Gray Niagaran in core and GR logs (Fig. 3). For both northern and southern shelf-slope reef complexes, the A-1 Carbonate toe position is defined by Brown Niagaran thickness between 3 and 15 m (10–50 ft). Because individual reef complexes within the basin vary in thickness, a standard isopach cutoff was not applied to define the A-1 Carbonate reef crest position. For example, the reef crest position in the Columbus III reef complex is defined by Brown Niagaran thickness >107 m (350 ft), whereas the reef crest in the C-21 reef complex is defined by a thickness >122 m (400 ft; Fig. 3). The A-1 Carbonate reef flank position is located between the reef crest and reef toe positions. The depositional

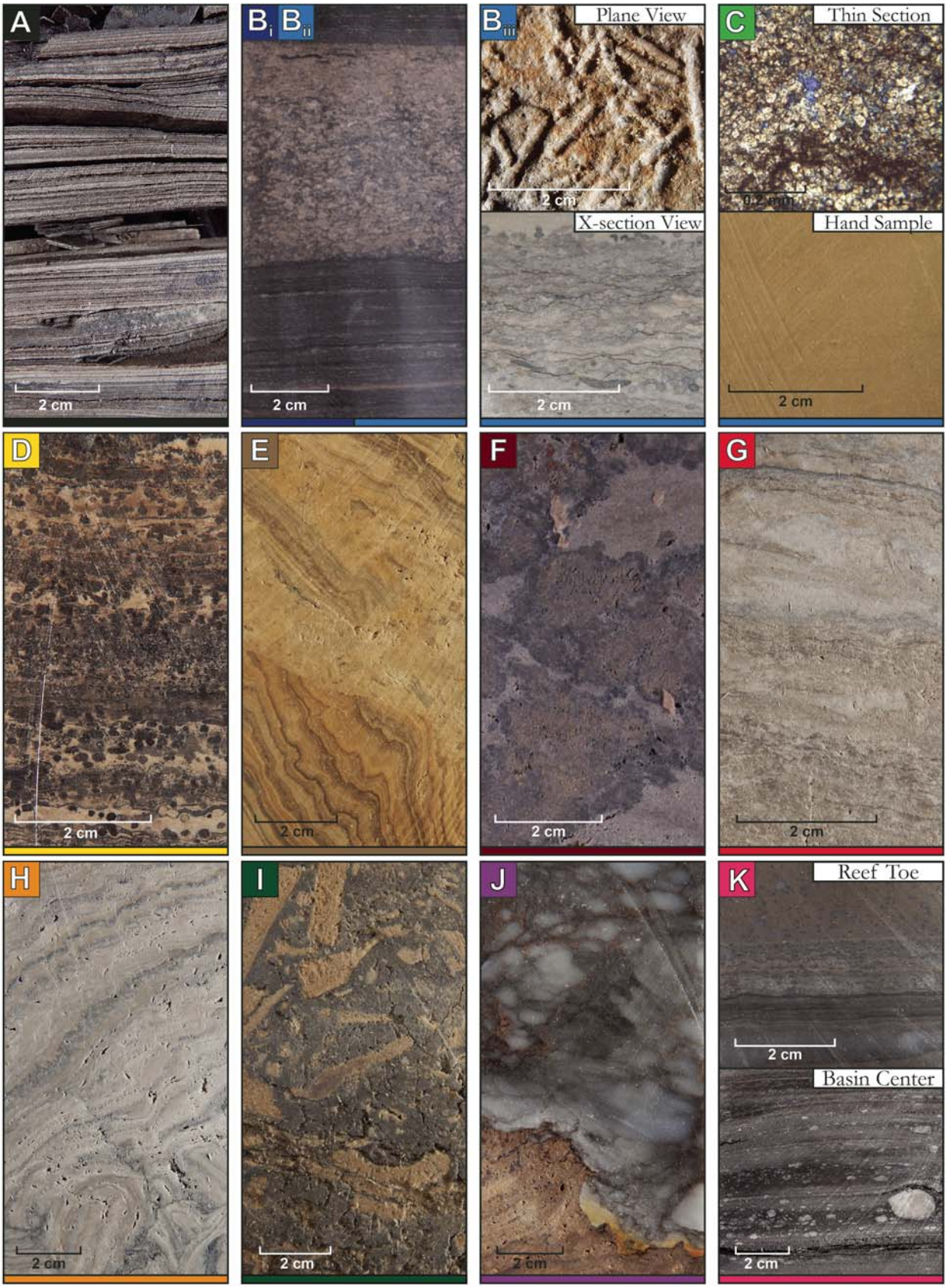
A
2 cm
Bi Bii
2 cm
Biii
Plane View
2 cm
X-section View
2 cm
C
Thin Section
Hand Sample
2 cm
D
2 cm
E
2 cm
F
2 cm
G
2 cm
H
2 cm
I
2 cm
J
2 cm
K
Reef Toe
2 cm
Basin Center
2 cm

Figure 2.

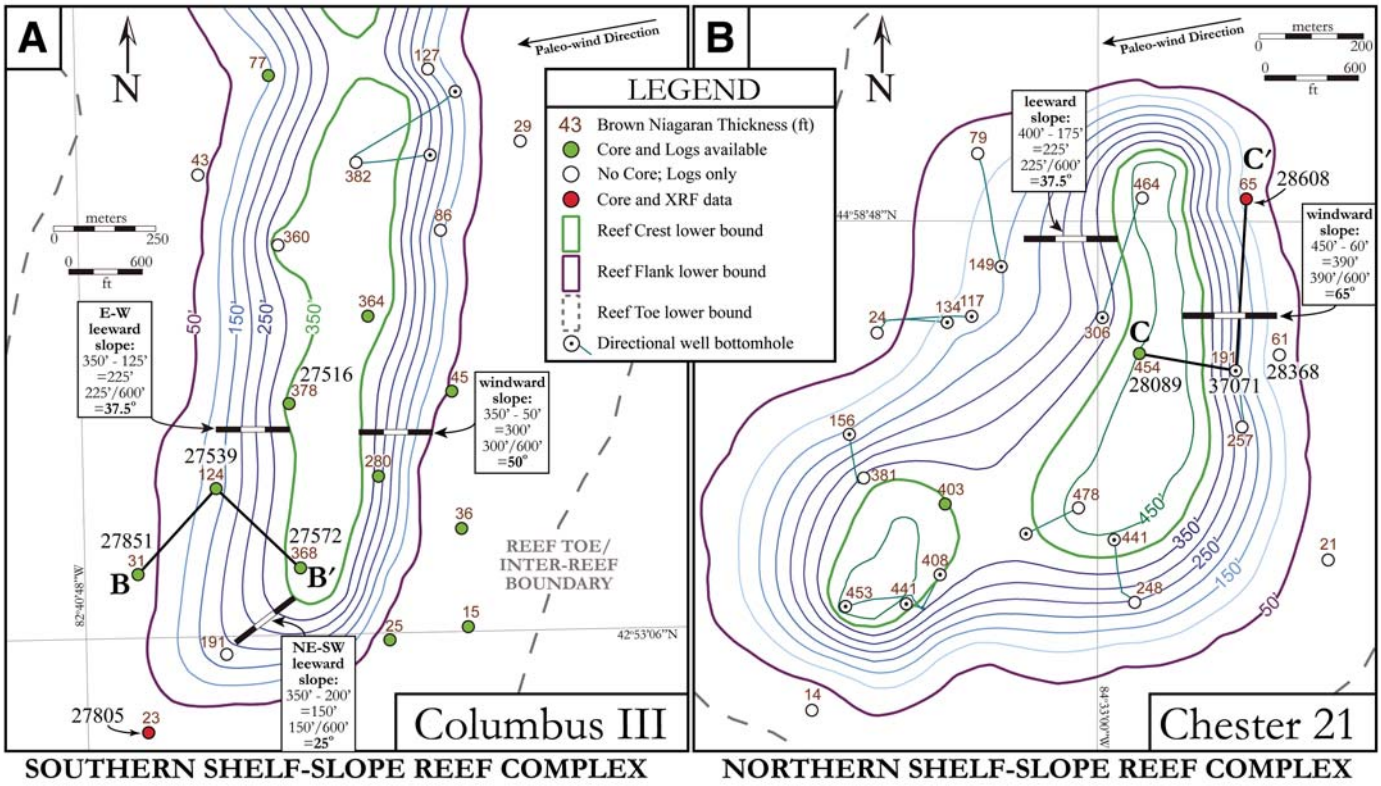

Figure 3. (A) Brown Niagaran isopach map of the southern shelf-slope Columbus III reef complex. Due to the influence of Brown Niagaran paleotopography on Salina deposition, the A-1 Carbonate was divided into five paleotopographic locations: (1) reef crest, (2) reef flank, (3) reef toe, (4) shelf-slope interreef, and (5) basin center. The B–B′ cross-section line represents the stratigraphic cross section in Figure 4A. (B) Brown Niagaran isopach map of the northern shelf-slope Chester 21 reef complex. The C–C′ cross-section line represents the stratigraphic cross section in Figure 4B. Permit numbers are displayed in black, and Brown Niagaran thicknesses are in brown. Calculated windward and leeward slopes are displayed for each complex based on a dominant easterly to northeasterly paleowind direction (from Rine et al., 2017). Refer to Figure 1A for reef complex locations. Note: Units are shown in feet. XRF—X-ray fluorescence.

Figure 2. Core photographs of representative lithofacies observed in the A-1 Carbonate throughout the Michigan Basin: (A) argillaceous carbonate laminate, basin center (#59271, 2203.1 m [7228 ft]); (B_i) thinly laminated mudstone and (B_{ii}) normally graded mudstone, Columbus III reef toe (#27669, 975.7 m [3201 ft]); (B_{iii}) laminated peloidal wackestone, BRM reef toe (#23797, 765.0 m [2510 ft]); (C) crystalline dolomite, Columbus III reef toe (#27851, 947.3 m [3108 ft]); (D) peloidal packstone, C-21 reef flank (#28608, 1823.3 m [5982 ft]); (E) stromatolitic rudstone, Columbus III reef flank (#27539, 938.2 m [3078 ft]); (F) thrombolitic bindstone, Columbus III reef crest (#27572, 869.6 m [2853 ft]); (G) laminated agglutinated thrombolitic-stromatolite, Columbus III reef crest (#27572, 863.2 m [2832 ft]); (H) white crinkly laminated stromatolitic bindstone, Columbus III reef crest (#27516, 865.9 m [2841 ft]); (I) stromatolitic floatstone, Columbus III reef flank (#27539, 931.5 m [3056 ft]); (J) enterolithic anhydrite, Columbus III reef flank (#27539, 927.2 m [3042 ft]); and (K) nodular anhydritic mudstone, Columbus III reef toe (#27805, 957.4 m [3141 ft]; top), and nodular anhydritic mudstone, basin center (#59271, 2204.6 m [7233 ft]; bottom).

slope of the reef flank position typically ranges 15°–37.5° on the western (leeward) side of the reef complexes, and 40°–65° on the eastern (windward) side. Figure 3 shows steeper slope angles on the reef flanks in the northern shelf-slope C-21 reef complex than in the southern shelf-slope Columbus III reef complex. The shelf-slope interreef position occurs between reef toes on adjacent complexes. Its thickness ranges from 2 to 3 m (7–10 ft). The basin center position is assigned to A-1 Carbonate deposits located downdip of the northern and southern shelf-slope reef belts (Fig. 1A). Deposits in this position invariably overlie the A-1 Salt unit, which is >50 m thick.

Southern Shelf-Slope Lithofacies Associations

In the Columbus III reef toe core (Fig. 4A), the Upper A-1 Carbonate (20.7 m) is ~3× thicker than the Lower A-1 Carbonate (6.4 m). These units are separated by a 5.5-m-thick anhydrite-rich interval referred to as the Rabbit Ear Anhydrite. The Lower A-1 Carbonate consists of alternating normally graded mudstone (lithofacies B_{ii}) and laminated peloidal wackestone (lithofacies B_{iii}). The Rabbit Ear Anhydrite consists of interbedded nodular anhydritic mudstone (lithofacies K) and normally graded

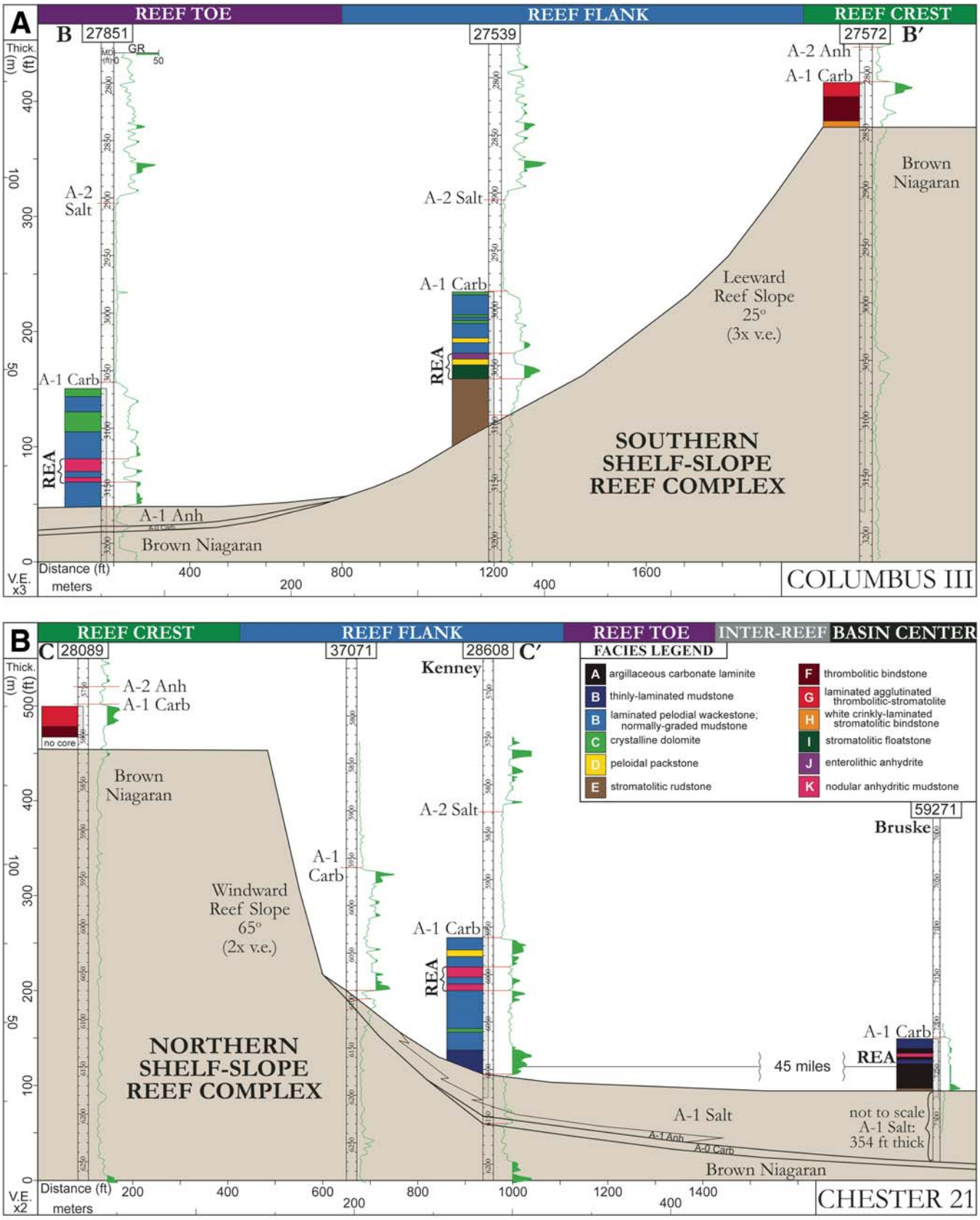
A
REEF TOE
REEF FLANK
REEF CREST
B
27851
27539
27572
B′
Thick. (m) (ft)
GR
A-2 Anh
A-1 Carb
A-2 Salt
Brown Niagaran
Leeward Reef Slope 25° (3x v.e.)
A-1 Carb
REA
SOUTHERN SHELF-SLOPE REEF COMPLEX
A-1 Anh
Brown Niagaran
Distance (ft)
meters
V.E. x3
COLUMBUS III
B
REEF CREST
REEF FLANK
REEF TOE
INTER-REEF
BASIN CENTER
C
28089
37071
28608
C′
Kenney
FACIES LEGEND
A argillaceous carbonate laminite
B thinly-laminated mudstone
B laminated pelodial wackestone; normally-graded mudstone
C crystalline dolomite
D peloidal packstone
E stromatolitic rudstone
F thrombolitic bindstone
G laminated agglutinated thrombolitic-stromatolite
H white crinkly-laminated stromatolitic bindstone
I stromatolitic floatstone
J enterolithic anhydrite
K nodular anhydritic mudstone
59271
Bruske
A-2 Anh
A-1 Carb
no core
Brown Niagaran
A-2 Salt
A-1 Carb
Windward Reef Slope 65° (2x v.e.)
A-1 Carb
REA
NORTHERN SHELF-SLOPE REEF COMPLEX
45 miles
A-1 Carb
REA
A-1 Salt
not to scale
A-1 Salt: 354 ft thick
A-1 Anh
A-0 Carb
Brown Niagaran
Distance (ft)
meters
V.E. x2
CHESTER 21

Figure 4.

mudstone (lithofacies B_{ii}). The Upper A-1 C is composed of normally graded mudstone (lithofacies B_{ii}) and crystalline dolomite (lithofacies C). In thin section, the only observable features in the crystalline dolomite (lithofacies C) are small dolomite rhombs (~40–80 µm wide) that host intercrystalline pore space (Fig. 2). The crystalline dolomite (lithofacies C) is often interbedded with the normally graded mudstone (lithofacies B_{ii}) and laminated peloidal wackestone (lithofacies B_{iii}).

In the Columbus III reef flank core (Fig. 4A), the Upper A-1 Carbonate (16.8 m) is ~1.5× thicker than the Lower A-1 Carbonate (10.4 m). These units are separated by a 5.8-m-thick Rabbit Ear Anhydrite. Here, the Lower A-1 Carbonate consists of a stromatolitic rudstone (lithofacies E), which is heavily oil-stained (Fig. 2). The Lower A-1 Carbonate stromatolitic rudstone (lithofacies E) grades vertically into the overlying basal Rabbit Ear Anhydrite stromatolitic floatstone (lithofacies I), which is matrix supported. The gradational transition from Lower A-1 Carbonate to Rabbit Ear Anhydrite can also be observed in GR logs, showing a gradual increase from the base of the A-1 Carbonate (3092 ft [942 m]) to the top of the stromatolitic floatstone (lithofacies I) interval (~3049 ft [929 m]; Fig. 4A). The stromatolitic floatstone (lithofacies I) is directly overlain by a thin (1.5 m) peloidal packstone (lithofacies D), which itself is overlain by an enterolithic anhydrite (lithofacies J). The Upper A-1 Carbonate in this core is composed of: normally graded mudstone (lithofacies B_{ii}), laminated peloidal wackestone (lithofacies B_{iii}), peloidal packstone (lithofacies D), and crystalline dolomite (lithofacies C), which are listed according to decreasing GR. While facies associated with the reef toe position consist of varying degrees of dolomitization, both the Lower and Upper A-1 Carbonate deposits associated with the reef flank position are completely dolomitized.

In the Columbus III reef crest core (Fig. 4A), the A-1 Carbonate is composed of a white, crinkly laminated stromatolitic bindstone (lithofacies H), overlain by a thrombolitic bindstone (lithofacies F), and capped by a laminated, agglutinated thrombolitic-stromatolite (lithofacies G). The uppermost laminated, agglutinated thrombolitic-stromatolite (lithofacies G) exhibits a distinctive high-GR signature, which is observed in both the northern and southern shelf-slope A-1 Carbonate reef crest positions.

Figure 4. (A) 3× vertically exaggerated stratigraphic cross section of the western (leeward) side of the Columbus III reef complex. The cross section is hung on the Gray Niagaran surface. In the reef crest and reef flank positions, the Brown Niagaran paleotopographic surface represents the unconformable contact between the Brown Niagaran and A-1 Carbonate. In the reef toe position, the A-1 Carbonate unconformably overlies the A-1 Anhydrite. Gamma-ray (GR) logs are displayed in green on a 0–50 API (American Petroleum Institute) unit scale (shaded >25). Cored intervals are highlighted gray in the measured depth track. (B) 2× vertically exaggerated stratigraphic cross section of the eastern (windward) side of the Chester 21 reef complex, including the basin center Bruske #1-26A core. Refer to Figures 1A and 3 for well locations. Note: Units are shown in feet (45 mi = 72 km; 354 ft = 108 m). REA—Rabbit Ears Anhydrite; v.e.—vertical exaggeration.

Northern Shelf-Slope Lithofacies Associations

The facies described for the southern shelf-slope Columbus III reef complex are similar to those in the northern shelf-slope C-21 reef complex. The reef crest core (Fig. 4B) is composed of laminated, agglutinated thrombolitic bindstone (lithofacies G) and thrombolitic bindstone (lithofacies F). In the northern shelf-slope C-21 reef flank position (Fig. 4B), the core consists of a Lower A-1 Carbonate (26.8 m) that is ~3× thicker than the Upper A-1 Carbonate (9.4 m). These units are separated by a 7.6-m-thick Rabbit Ear Anhydrite (Fig. 4B). The Lower A-1 Carbonate is ~3× thicker than the Upper A-1 Carbonate in the northern trend. This contrasts to what is observed in the southern trend, where the Upper and Lower A-1 Carbonate are nearly equal. The lowermost 9 m section of the Lower A-1 Carbonate consists of thinly laminated mudstone (lithofacies B_i) that is slightly argillaceous and pyritic and displays distinct fissile parting. The remainder of the overlying Lower A-1 Carbonate is composed mostly of normally graded mudstone (lithofacies B_{ii}) with clasts of peloids, stromatolites, and brachiopods. The Rabbit Ear Anhydrite consists of nodular anhydritic mudstone (lithofacies K), similar to that observed in the Columbus III reef toe position (Fig. 4A). In the Upper A-1 Carbonate, peloid grains are prevalent, with facies ranging between laminated peloidal wackestone (B_{iii}) to peloidal packstone (D), as well as normally graded mudstone (B_{ii}).

Basin Center Lithofacies Associations

In the basin center core (Fig. 4B) the majority of the Lower A-1 Carbonate is composed of argillaceous carbonate laminite (lithofacies A), composed of millimeter-scale, planar laminations composed of alternating layers of gray micrite with black carbonaceous and argillaceous mudstone (Fig. 2). Fissile parting is common along laminations, which results in very thin discs in whole core (this facies has been referred to as the "poker chip facies" in previous studies). The lowermost meter of the A-1 Carbonate is composed of thin, millimeter-scale laminations of anhydrite and carbonate that transition vertically into a thin interval of stromatolitic rudstone (lithofacies E). The bottom meter of the A-1 Carbonate also corresponds to the highest GR values in the basin center core. The Rabbit Ear Anhydrite in the basin center core is composed of slightly thicker (centimeter-scale) laminations of thinly laminated mudstone (lithofacies B_i), as well as a thinly laminated anhydritic mudstone (lithofacies K). Anhydrite fabrics in this core are characterized by millimeter-wide nodules elongated parallel to bedding that occur within individual mudstone laminations (Fig. 2). The Upper A-1 Carbonate in the basin center core is composed of centimeter-scale laminations of thinly laminated mudstone (lithofacies B_i) that are thicker than the millimeter-scale, argillaceous carbonate laminations observed in the Lower A-1 Carbonate (facies A).

ED-XRF Elemental Data

In general, all three cores that were analyzed with ED-XRF exhibited a general decrease in GR, K, Si, Al, and Fe from the

base to the top of the A-1 Carbonate (Figs. 5, 6, and 7). All three cores also exhibited elevated concentrations of S and Sr associated with anhydrite-rich facies of the Rabbit Ear Anhydrite, as well as the overlying A-2 Anhydrite and underlying A-1 Anhydrite. Elevated concentrations of Sr, Mo, and Ni correspond to dolomitic intervals, such as the crystalline dolomite facies (C) in the southern reef toe Winn core (Fig. 5).

The southern reef toe Winn core is almost entirely dolomitized in the Lower A-1 Carbonate (Fig. 5), which is reflected in high Mg values (10–13 wt%). Pyrite-lined bedding planes in the Lower A-1 Carbonate correspond to elevated levels of Fe and S. Pyritized surfaces, it should be noted, were recognized petrographically only after increases in Fe and S were recorded by XRF. Thin argillaceous carbonates that exhibit fissile parting (e.g., lithofacies B_i and A) correspond to zones of elevated Si, Al, and K.

Dolomite is less abundant in the northern reef flank Kenney core as compared to the southern reef toe Winn core (Fig. 6).

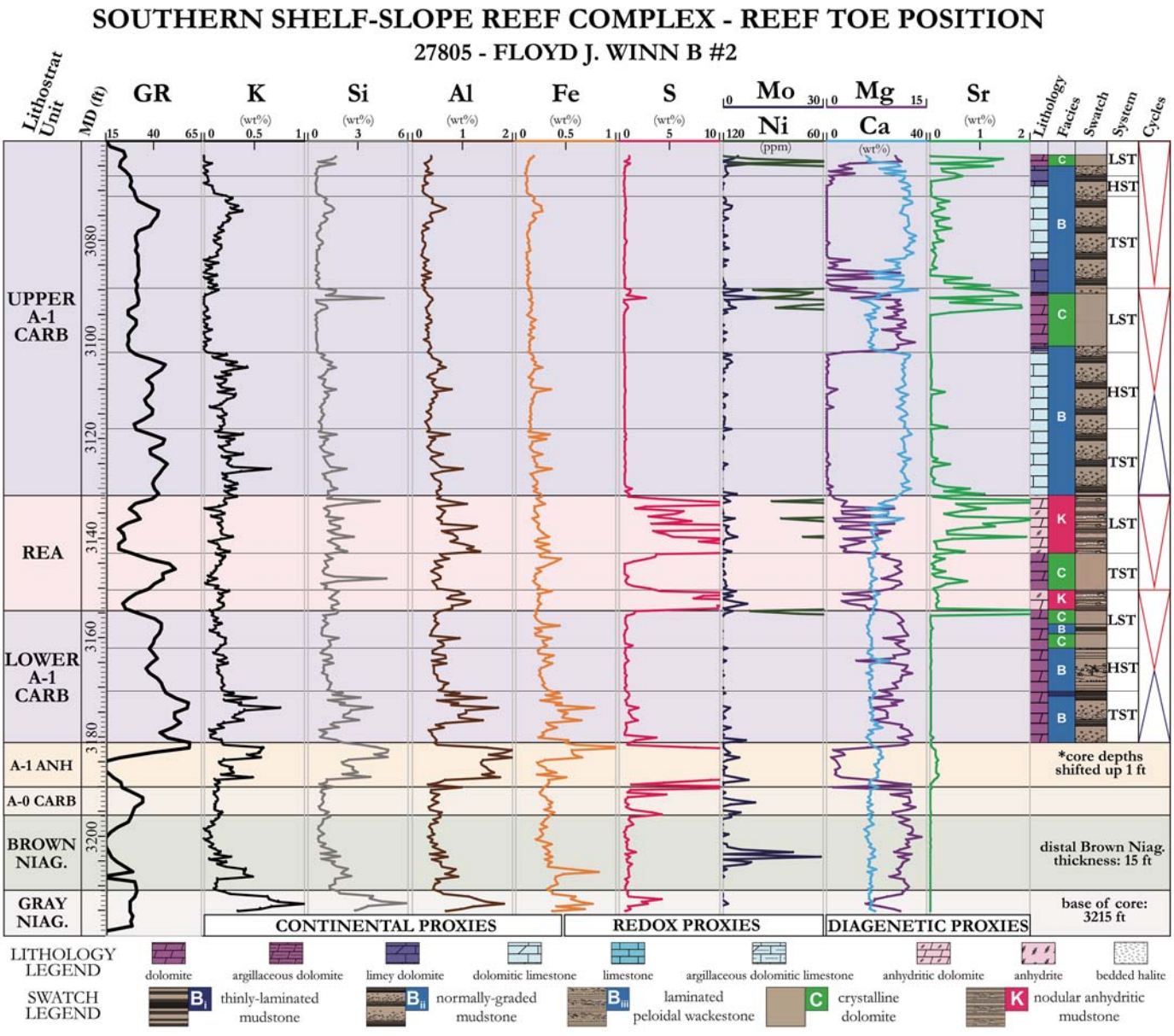

Figure 5. Core profile for the Floyd J. Winn B #2 well located on the western reef toe position of the southern shelf-slope Columbus III reef complex (see Fig. 3A). Displayed (left to right) are lithostratigraphic units, measured depth (MD; ft), gamma ray (GR, API units), elemental data collected from energy-dispersive X-ray fluorescence spectrometry (ED-XRF), lithology, facies, and sequence stratigraphic interpretations. Note: Units are shown in feet (1 ft = 0.3 m; 15 ft = 4.5 m; 3215 ft = 980 m). REA—Rabbit Ears Anhydrite; LST—lowstand systems tract; TST—transgressive systems tract; HST—highstand systems tract. See Table 2 or Figure 4 legend for facies.

The basal portion of the Lower A-1 Carbonate in the Kenney core, which is characterized by elevated GR values, also shows increased amounts of Fe, Si, Al, and K. Potassium, one of three radioactive elements recorded by the GR logging tool (K, U, Th), closely tracks the GR in all three cores. Distinct decreases in GR, K, Si, Al, and Fe occur around 6080 ft (1853 m), a depth that marks a shift from the argillaceous thinly laminated mudstone (facies B_i) to mostly normally graded mudstone (facies B_{ii}). Similar to the southern reef toe core, the Rabbit Ear Anhydrite in the northern reef flank core has elevated concentrations of S and Sr.

In the basin center Bruske core, the basal 1 m section of the Lower A-1 Carbonate is composed of anhydritic dolomite (Fig. 7). This thin zone is also characterized by high K, Si, Al, Fe, S, and Mo concentrations. The Rabbit Ear Anhydrite in the Bruske core, similar to the two other XRF cores, exhibits elevated S and Sr concentrations associated with anhydrite-rich lithofacies. Only the upper Rabbit Ear Anhydrite, however, has anhydrite fabrics visibly observable in core. The lower Rabbit Ear Anhydrite, in contrast, is composed of thinly laminated mudstone (facies B_i), which has

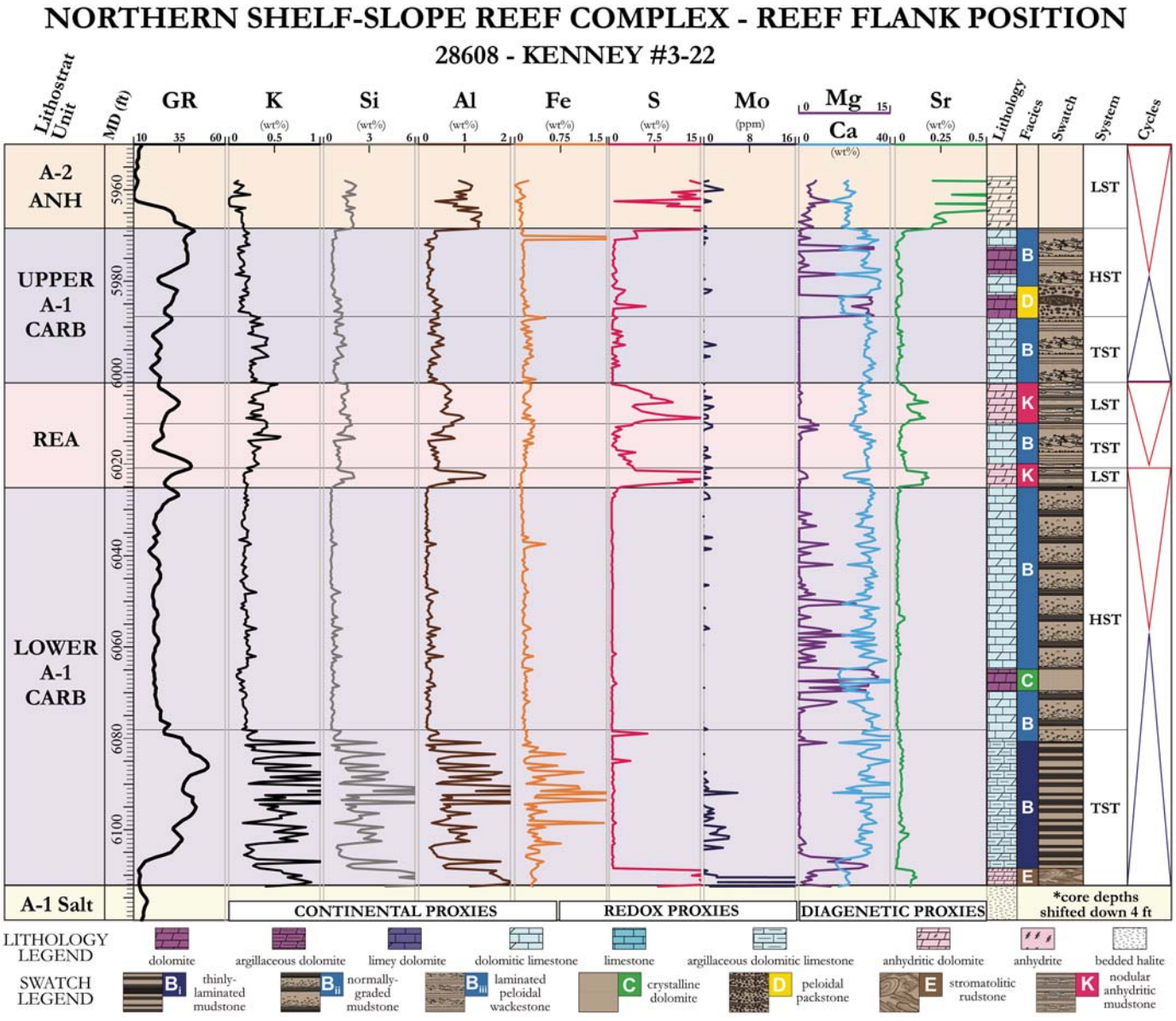

Figure 6. Core profile for the Kenney #3-22 well located on the eastern reef flank position of the northern shelf-slope Chester 21 reef complex (see Fig. 3B). Displayed (left to right) are lithostratigraphic units, measured depth (MD; ft), gamma ray (GR, API units), elemental data collected from energy-dispersive X-ray fluorescence spectrometry (ED-XRF), lithology, facies, and sequence stratigraphic interpretations. Note: Units are shown in feet (1 ft = 0.3 m; 4 ft = 1.2 m). REA—Rabbit Ears Anhydrite; LST—lowstand systems tract; TST—transgressive systems tract; HST—highstand systems tract. See Table 2 or Figure 4 legend for facies.

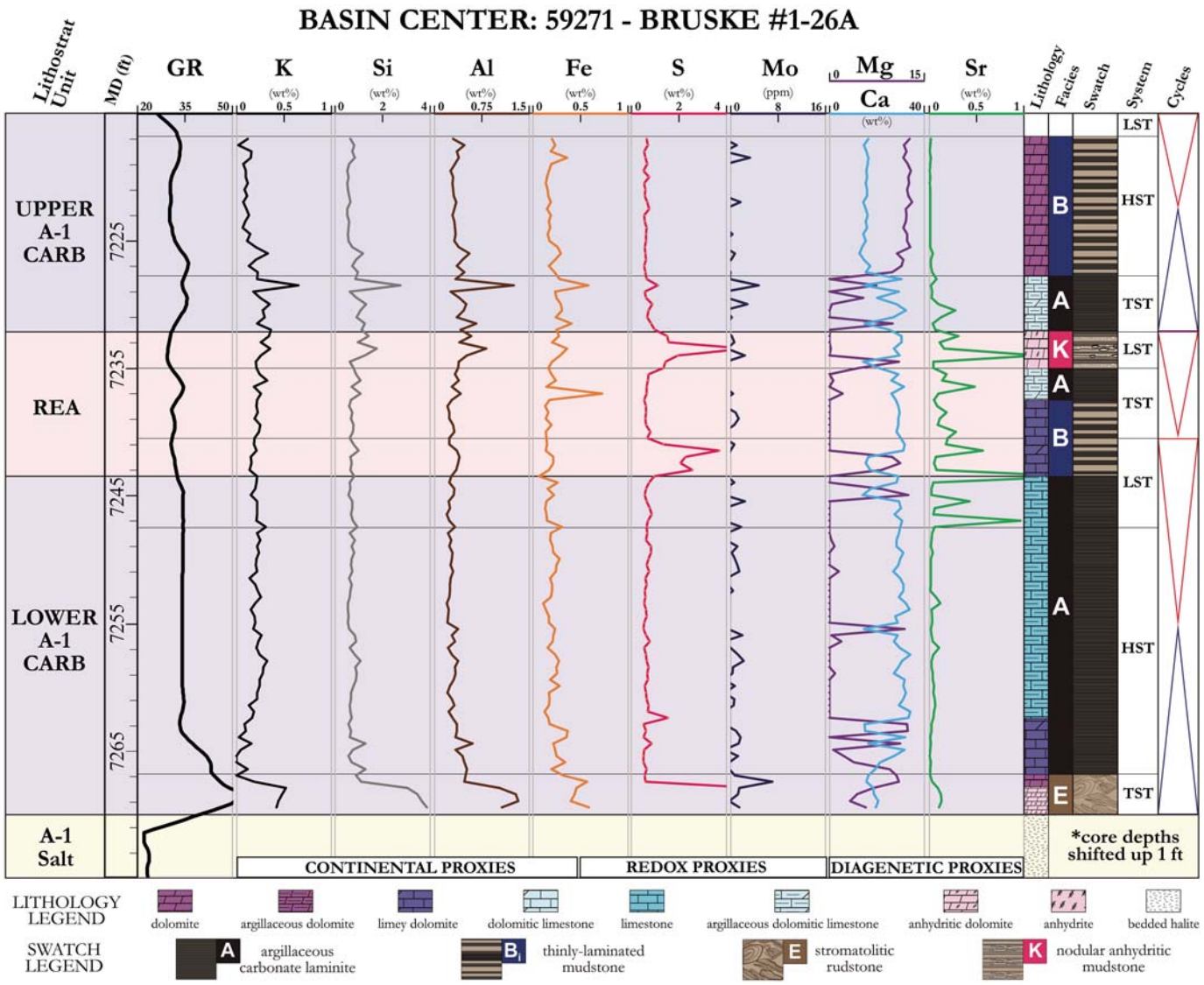

Figure 7. Core profile for the basin center Bruske #1-26A well (see Fig. 1A). Displayed (left to right) are lithostratigraphic units, measured depth (MD; ft), gamma ray (GR, API units), elemental data collected from energy-dispersive X-ray fluorescence spectrometry (ED-XRF), lithology, facies, and sequence stratigraphic interpretations. Note: Units are shown in feet (1 ft = 0.3 m). REA—Rabbit Ears Anhydrite; LST—lowstand systems tract; TST—transgressive systems tract; HST—highstand systems tract. See Table 2 or Figure 4 legend for facies.

high values of both S and Fe associated with petrographically observed pyrite.

INTERPRETATION AND DISCUSSION

A-1 Carbonate Depositional Models

Complementary depositional models are presented in Figure 8 for the Upper and Lower A-1 Carbonates and the Rabbit Ear Anhydrite. The A-1 Carbonate depositional model (Fig. 8A) illustrates how nine of the 13 observed lithofacies are distributed along a dip profile. The A-1 Carbonate model describes carbonate deposition during relative sea-level highs and moderate basin restriction. The Rabbit Ear Anhydrite depositional model (Fig. 8B) includes three of the 13 observed lithofacies. This model describes evaporite deposition during relatively low sea levels and intense basin restriction. Both models are intended to show lateral facies assemblages for contemporaneous sedimentation across the basin in different depositional environments. Each A-1 Carbonate depositional environment is discussed in detail next. It should be noted that the crystalline dolomite (C) facies was not assigned to either depositional model because it is devoid of any recognizable depositional fabric. Facies C does exhibit elevated concentrations of Si, S, Mo, Ni, and Sr (Fig. 5), which is similar to the elemental signature of the Rabbit Ear Anhydrite, and the A-1

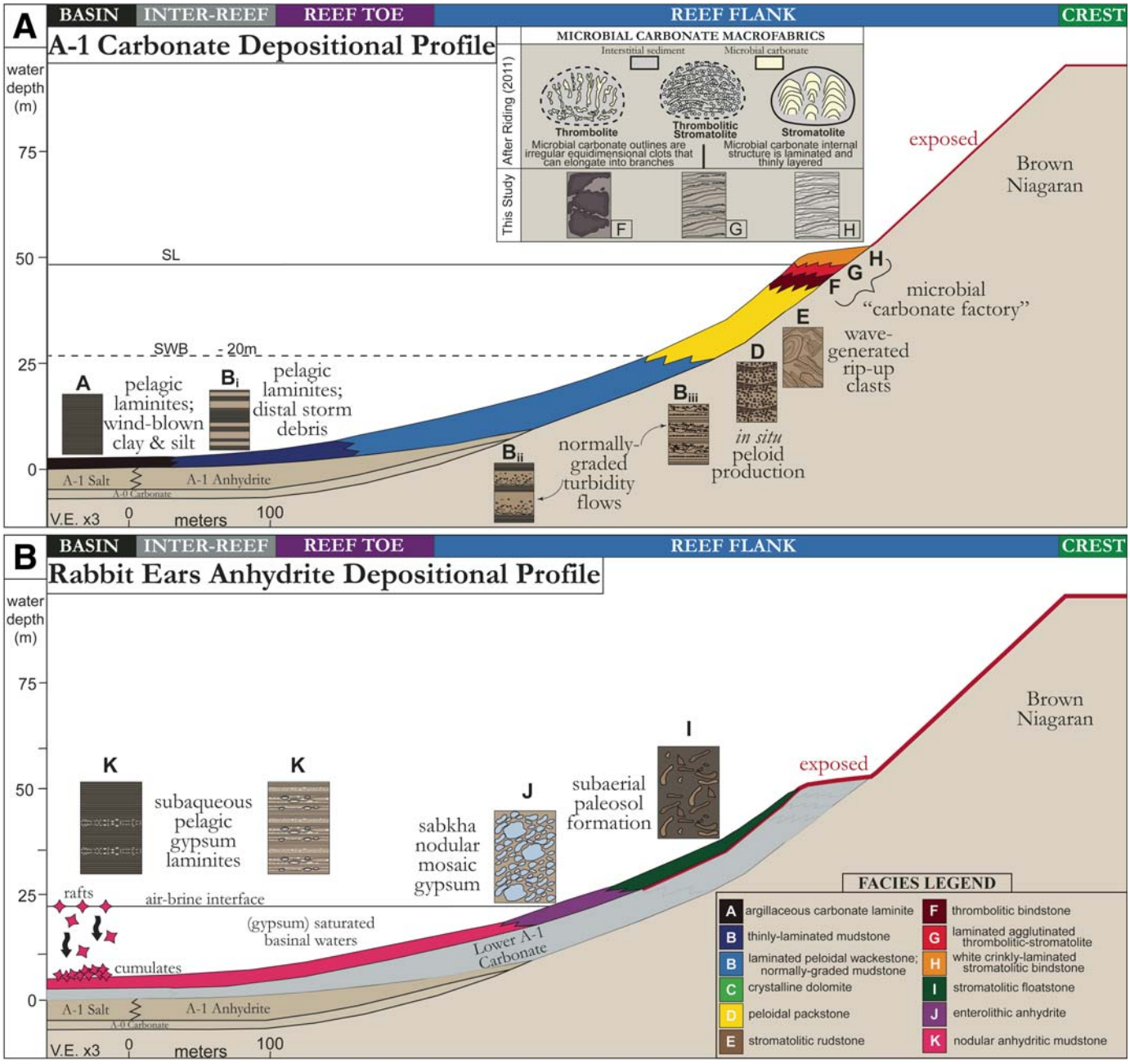

Figure 8. (A) Depositional model for lateral facies distributions during A-1 Carbonate deposition. Included is a comparison of microbial carbonate macrofabrics described in Riding (2011) to those in A-1 Carbonate facies observed in this study. (B) Depositional model for lateral facies distributions during Rabbit Ears Anhydrite deposition. SL—sea level; SWB—storm wave base; V.E.—vertical exaggeration.

and A-2 Anhydrite units. Despite its geochemical similarity to the Rabbit Ear Anhydrite, this purely diagenetic facies was omitted from both depositional models.

Peritidal and Shallow Subtidal Environments

In contrast to the carbonate factory in the underlying Niagaran, which is dominated by normal-marine facies (e.g., Mantek, 1973; Mesolella et al., 1974; Gill, 1973; Huh, 1973; Sears and Lucia, 1979), the carbonate factory in the A-1 Carbonate is dominated by more restricted facies (Fig. 8A). In the reef crest position, the A-1 Carbonate carbonate factory is characterized by the white, crinkly laminated stromatolitic bindstone, thrombolitic bindstone, and laminated, agglutinated thrombolitic-stromatolite facies. All three facies are representative of deposition in supratidal to shallow subtidal settings, a conclusion also reached in previous studies (Budros and Briggs, 1977; Gill, 1977).

In general, there is a clear transition to deeper-water facies down depositional slope. The white, crinkly laminated stromatolitic bindstone is characterized by alternating layers of in-place stromatolites and flat-pebble conglomerates containing stromatolite lithoclasts. This facies is only present in the reef crest position, and it is interpreted to reflect high-energy, intertidal conditions. While this facies likely formed locally in the reef crest position, large stromatolite lithoclasts found in the stromatolitic rudstone facies (Fig. 2) downdip in the reef flank position appear to have been transported, as evidenced by the presence of randomly oriented, pebble-size, angular stromatolite clasts. Further downdip in the reef toe position, beds of the normally graded mudstone are characterized by scoured bases rich in coarser-grained material composed of millimeter-scale stromatolite clasts, brachiopods, and pellets (Fig. 2). The steep sides of these reef complexes (15°–65°) support an interpretation where downslope transport played a critical role in distributing material (Playton et al., 2010) from the carbonate factory at the reef crest to the reef flank, reef toe, and interreef positions.

In the reef crest position, the thrombolitic bindstone is texturally and genetically different than the white, crinkly laminated stromatolitic bindstone. Though these facies have been observed to occur in similar environments (Riding, 2011), thrombolites are typically associated with shallow, subtidal conditions, whereas stromatolites are more representative of high-energy, intertidal settings (Feldmann and McKenzie, 1997). This interpretation is supported by vertical facies assemblages, which show: (1) that stromatolites are the first A-1 Carbonate facies recognized in the reef crest position above the Niagaran unconformity as sea level began to rise, and (2) that the thrombolites invariably overlie the stromatolites (Fig. 4A), appear to be in growth position, and lack textural evidence of higher-energy conditions.

The laminated, agglutinated thrombolitic-stromatolite is generally coarser than the other microbial facies, has abundant intercalated, elongated peloids that are not observed in the other facies, and always occurs directly below the A-2 Anhydrite. These observations point to a distinctive depositional environment for this facies, but it is unclear if it occupies a unique position along the dip profile.

Deep-Water Environments

In contrast to previous studies, which interpreted the entire A-1 Carbonate as a shallow-water deposit, we posit that the majority of A-1 Carbonate facies not located in the reef crest position are of deep-water origin. The majority of the lithofacies in the reef flank and reef toe positions are interpreted as sediment gravity flows. Individual beds in the reef flank and toe positions thin into the basin, are normally graded, and are bounded by scour surfaces. The bases of the beds are characterized by the presence of coarse peloids, brachiopods, and stromatolite clasts (Fig. 2).

Further basinward, in the interreef and basin center positions, the presence of argillaceous carbonate laminite (A) and thinly laminated mudstone (B_i) facies supports a deeper-water pelagic origin. These particular facies were possibly formed by a combination of the following processes:

(1) Detrital carbonate was delivered to the basin from the surrounding shelf-slope reef complexes, as evidenced by the dominance of fine-grained carbonate material and lack of fossil fragments or peloids. Similar increases in carbonate mud coupled with a decrease in grains associated with gravity-driven deposits are observed with increasing distance away from carbonate growth escarpments in the Canning Basin of Western Australia (Playton et al., 2010). Gravity-driven deposition down the slope is the envisioned mechanism for transportation of detrital carbonate to more basinward environments.

(2) Inorganic precipitation of calcite occurred at the air-brine interface, and pelagic settling to the basin floor ensued. This type of inorganic cumulate sedimentation has been observed in ancient evaporitic carbonate basins around the world (Warren, 2016). An example of a deep-water pelagic, inorganic carbonate laminite can be found in the Northern Basin of the Dead Sea, Israel, where Garber et al. (1987) described alternating layers of light and dark millimeter-scale laminae that accumulated in more than 350 m of water depth.

(3) Windblown silt (quartz) and clays (illite, chlorite) from terrigenous sources surrounding the Michigan Basin (e.g., Canadian Shield to the north). This is evidenced by increased elemental concentrations of K, Si, Al, and Fe associated with facies A and B_i in the basin center and reef flank positions. Wells located closer to the basin margin are observed to have higher concentrations of these elements, which supports a continental source for these materials (Figs. 5–7).

(4) Pelagic accumulation of organic carbon from the water column occurred in a deep (>100 m), dysoxic to suboxic bottom-water environment. Dysoxic bottom-water conditions are inferred from higher concentrations of redox-sensitive elements, such as Mo (Tribovillard et al., 2006; Algeo and Rowe, 2012), as well as Fe and S in the form of pyrite (FeS_2).

The approach used here relies on previous sedimentological-geochemical studies that identified strong trends and relationships between elemental concentrations and paleoenvironmental conditions in siliciclastic mudrocks (e.g., Tribovillard et al., 2006; Algeo and Rowe, 2012; Al Ibrahim, 2015; Wu and Boak, 2015; Turner et al., 2016). Because the deep-water environments discussed for A-1 Carbonate deposition can be similar to those hosting siliciclastic deposition, many of the elemental proxies used to interpret mudrocks (summarized in Turner et al., 2016; Table 3) can be appropriately applied to A-1 Carbonate facies. Such proxies have been used successfully in other carbonate systems (Algeo and Maynard, 2008; Algeo and Rowe, 2012; Banner, 1995), thus lending credence to the method used here. Moreover, many of the elemental concentrations correlate well with observed facies changes and GR signatures, which suggests that the signatures are, in fact, recording useful information about basin conditions.

TABLE 3. COMPARISON OF ELEMENTAL DATA & ENVIRONMENTAL PROXIES

Mudrocks			*Carbonates / Evaporites (this study)*		
Element	Proxy	Ref.	Element(s)	Potential mineralogy	Observations
Calcium (Ca)	Carbonate source and phosphate	† ☆	**Depositional**		
Titanium (Ti)	Continental source and dust fraction	*	Continental: Si	$\mathbf{Si}O_2$ (*quartz*)	Si, Al, K associated with lowstand & early transgressive stages
Zirconium (Zr)	Continental source	z	Continental: Al, K	$\mathbf{K}\mathbf{Al}_2(\mathbf{Si}O_3\mathbf{Al}O_{10}(OH)_2$ (*illite*)	Gamma ray log tracks K
Strontium (Sr)	Carbonate source and phosphate	† ☆	Continental: Fe	$(Mg,\mathbf{Fe},Li,)_6\mathbf{Al}\mathbf{Si}_3O_{10}(OH)_8$ (*chlorite*)	
Silicon:Aluminum ratio (Si:Al)	Quartz (biogenic and detrital)	‡ * ↓	Redox: Fe, S	$\mathbf{Fe}S_2$ (*pyrite*)	Pyrite observed in transgressive and highstand facies; anhydrite in lowstand
Aluminum (Al)	Continental source and dust fraction	† ‡	Redox: S	$Ca\mathbf{S}O_4$ (*anhydrite*)	
Potassium (K)	Clay and feldspar	†	Redox: trace elements Mo Ni	Associated with lowstand stages; sea-level fall results in basin restriction and basin-wide euxinic conditions	
Phosphorus (P)	Phosphate accumulation	†	**Diagenetic**		
Molybdenum (Mo)	Bottom water euxinia, redox sensitive	† §	Ca	$\mathbf{Ca}CO_3$ (*calcite*)	Associated with anhydrite & dolomite below anhydrite units; elevated Sr in restricted; possibly refluxing brines
Vanadium (V)	Bottom water anoxia, redox sensitive	†	Mg	$Ca\mathbf{Mg}(CO_3)_2$ (*dolomite*)	
			trace elements Sr	$\mathbf{Sr}SO_4$ (*celestite*)	

Note: References: †Tribovillard et al. (2006) *Sageman & Lyons (2004) ‡Pearce & Jarvis (1992) §Algeo & Rowe (2012) ↓Pearce et al. (1999) ☆Banner (1995) zBhatia & Cook (1986)

Rabbit Ear Anhydrite Depositional Model

Three of the 13 A1-C lithofacies identified only appear in the Rabbit Ear Anhydrite interval. These facies are interpreted to be a product of highly evaporative, gypsum-saturated, euxinic basin waters (discussed in the following). In general, the distinct gypsum fabrics (Fig. 8B) observed within the Rabbit Ear Anhydrite at the various positions (T-3; Fig. 9) are interpreted to reflect variations in water depth and intermittent exposure during a basinwide sea-level drawdown. The Rabbit Ear Anhydrite also exhibits different textural attributes between the southern and northern shelf slopes. The following sections describe the Rabbit Ear Anhydrite depositional environments from shallowest to deepest.

Subaerial Exposure and Paleosol Formation

The transition from the stromatolitic rudstone (E) to a stromatolitic floatstone (I) in the lower Rabbit Ear Anhydrite at the Columbus III reef flank position is interpreted to reflect a sea-level fall and shift from subaqueous carbonate deposition to subaerial exposure. Whereas facies E exhibits no textural evidence of subaerial exposure, facies I is characterized by a friable dark, greenish-brown matrix interpreted to represent windblown clay and silt delivered during exposure and paleosol formation (Fig. 8B). Although elemental data were not collected in facies I, high GR values likely reflect the presence of clay minerals, such as illite (Table 3). Clays are a likely source of radiogenic K responsible for the observed GR values in facies I (Fig. 4A). This is supported by strong correlations among elevated concentrations of K, high GR, and clay-rich lithofacies in the three cores with elemental data.

Sabkha Flat Deposition

Downdip from the paleosol, there is the enterolithic anhydrite (J) facies, which is referred to elsewhere as chicken-wire anhydrite. Based on mineralogical and textural similarities with sediments observed on modern sabkhas (e.g., Warren, 2016), facies J is interpreted to represent deposition in a sabkha setting. The model in Figure 8B illustrates this facies on the reef flank, but it is also observed in reef crest and reef toe positions. An example of Rabbit Ear Anhydrite enterolithic fabrics is observed in the upper Rabbit Ear Anhydrite in the Columbus III reef flank position (Fig. 2). Here, it is separated from the lower Rabbit Ear Anhydrite paleosol facies by a 1.5-m-thick, peloidal packstone (Fig. 4A) that is interpreted to signify a small sea-level increase. A facies shift suggestive of a relative deepening event during Rabbit Ear Anhydrite deposition is not unique to the reef flank position, as it is observed in the Rabbit Ear Anhydrite interval in all positions throughout the basin. In the Columbus III field, some wells exhibit three anhydrite-rich layers within the Rabbit Ear Anhydrite. In other localities, as many as five anhydrite-rich units can be observed within the Rabbit Ear Anhydrite (well #37818; R. Budros, 2017, personal commun.), most likely the result of localized, higher-order sea-level changes. Despite the observed variability of Rabbit Ear Anhydrite lithofacies across different paleotopographic positions basinwide, all cores contain sedimentological and geochemical evidence of two major regressions separated by a small transgression (Figs. 5–7 and 10).

Deep-Water Subaqueous Pelagic Gypsum "Rain"

In the reef toe position, enterolithic anhydrite is absent basinward of the sabkha fabrics. Instead, Rabbit Ear Anhydrite facies are characterized by millimeter-scale anhydrite nodules nested

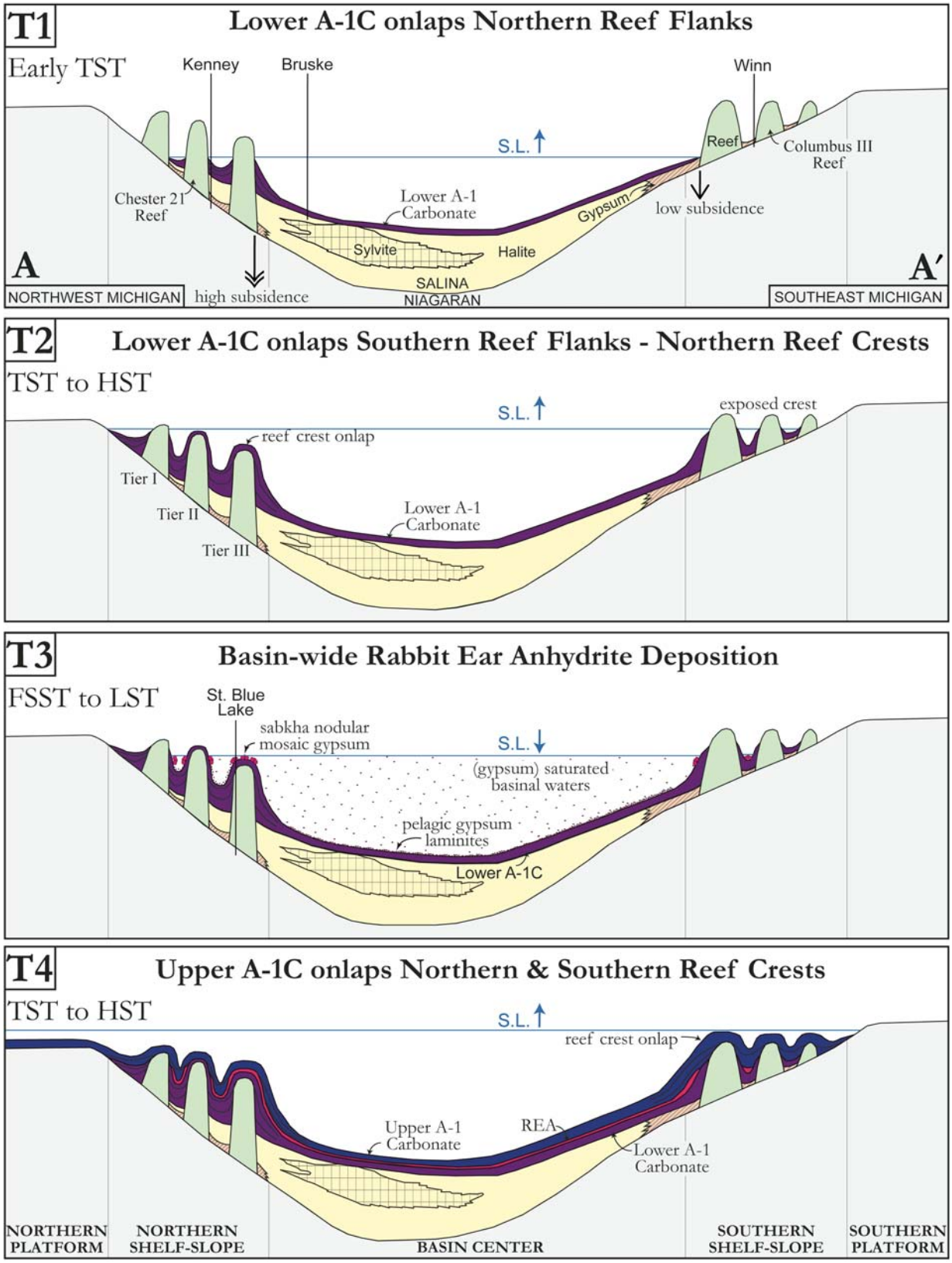

Figure 9. Generalized basinwide sequence stratigraphic model for deposition of the A-1 Carbonate (not to scale). Refer to the cross-section line A–A′ on Figure 1A. SL—sea level; LST—lowstand systems tract; TST—transgressive systems tract; FSST—falling stage systems tract; HST—highstand systems tract; REA—Rabbit Ears Anhydrite.

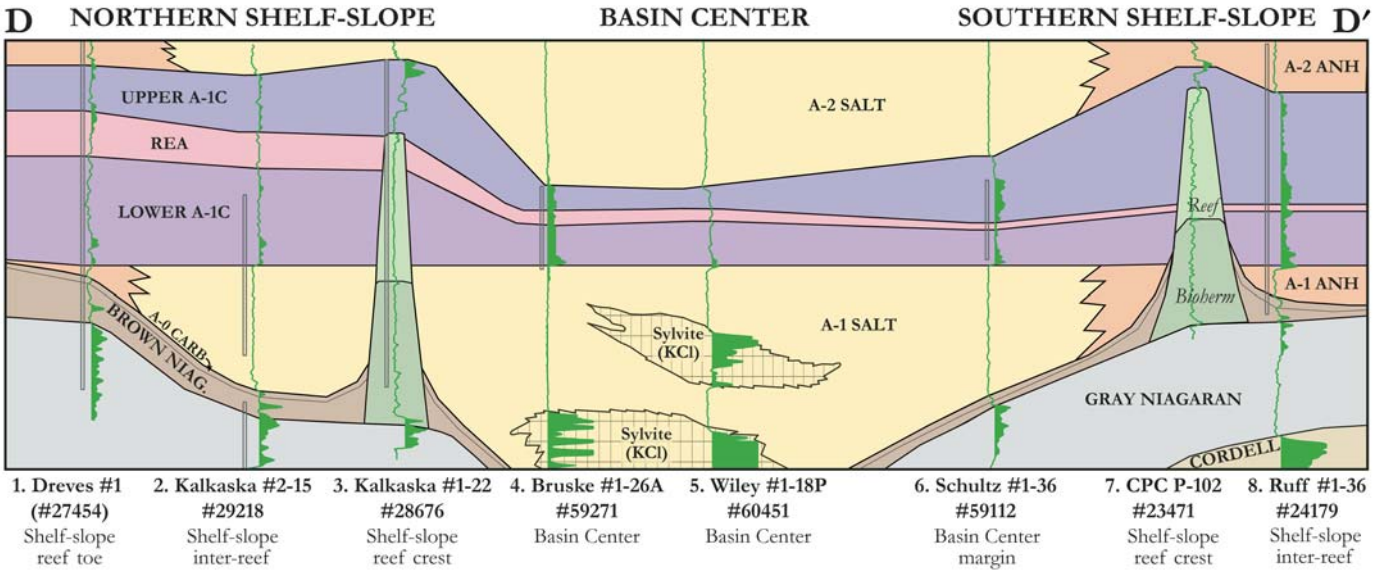

Figure 10. Basinwide cross section showing the stratigraphic relationships for the Niagara and Lower Salina units in the Michigan Basin. The stratigraphic cross section is flattened on the top of the A-1 Evaporite (A-1 Salt/A-1 Anhydrite), which best represents the paleotopographic surface prior to A-1 Carbonate deposition. Gamma-ray logs are shaded green for values >20. Tops were identified in core (cored interval noted left of GR) for all wells except 5 and 7. The cross section is not to scale horizontally. All wells except the reef crest wells (3 and 7) are on the same vertical scale. Reef crest wells are compressed vertically 1.5× to fit into the cross section. Refer to Figure 1A for well locations. REA—Rabbit Ears Anhydrite.

within a groundmass of laminated carbonate mudstone (nodular anhydritic mudstone). Because this lithofacies is observed in basin center positions (Fig. 10), which would have been in water depths >100 m during Rabbit Ear Anhydrite deposition, these millimeter-scale anhydrite nodules are interpreted to be subaqueous, pelagic gypsum. This interpretation is consistent with the subaqueous pelagic gypsum model proposed by Warren (2016). In this model, gypsum crystals precipitate at the air-brine interface as basin restriction increases. These clusters then fall as pelagic "gypsum rain" to form cumulate deposits on the seafloor (Fig. 8B).

Unique geochemical trends in the Rabbit Ear Anhydrite facies are significantly different than those observed in A-1 Carbonate facies. For example, Rabbit Ear Anhydrite facies always exhibit elevated amounts of S and Sr. Because Rabbit Ear Anhydrite deposition is interpreted to coincide with basin restriction during a regression, an increase in continental proxy element concentrations is predictable as the shoreline receded into the basin. Such increases in Si, Al, and Fe concentrations are clearly observed in the shelf-slope cores (Figs. 5 and 6), as well as in the basin center Bruske core in the upper Rabbit Ear Anhydrite interval (Fig. 7).

Deep-water Rabbit Ear Anhydrite facies are associated with increased concentrations of redox-sensitive elements, such as Mo and Ni (Table 3). A model for silled basins proposed by Algeo and Rowe (2012) linked basin restriction during lowstand conditions to increased concentrations of trace metals such as Mo and Ni. Increased concentrations of redox-sensitive elements were also observed by Turner et al. (2016) in the Woodford Shale lowstand mudrock deposits. They reported that lowstand systems tract deposits showed a correlation with higher concentrations of continentally derived elements. Transgressive systems tract deposits exhibited decreasing concentrations of continental proxy elements and generally low levels of restriction. Highstand systems tract deposits showed the lowest levels of restriction and increased continentally derived elements. The biggest difference between the findings of Turner et al. (2016) and what we observed in the A-1 Carbonate is that during highstand systems tract conditions, the A-1 Carbonate records lower concentrations of continental material, which we attribute to increased carbonate production rates.

Elevated concentrations of redox-sensitive trace elements, such as Mo and Ni, are observed in Rabbit Ear Anhydrite lowstand deposits, but the highest values are observed in the crystalline dolomite (C) facies of the Upper A-1 Carbonate (Fig. 5). Facies C also exhibits elevated concentrations of Sr, S, and Si, which, similar to the Rabbit Ear Anhydrite, are consistent with lowstand deposition and basin restriction, as discussed. Therefore, we propose that lowstands, associated with receded shorelines, euxinic water conditions, and increased concentrations of S and Sr, can be readily identified using ED-XRF data in both A-1 Carbonate and Rabbit Ear Anhydrite facies. In contrast to lowstand elemental signatures, transgressive systems tracts are associated with low carbonate concentrations (thinly laminated facies A and B), high concentrations of continental proxy elements, and abundant pyritized intervals promoted by the transition from

lowstand euxinic conditions to oxygenated highstand conditions. Last, highstand systems tracts are associated with the lowest concentrations of continental proxy elements and highest carbonate production rates, which are also recorded in basin center positions by thicker carbonate laminae in the Upper A-1 Carbonate compared to the Lower A-1 Carbonate (Fig. 7).

Sequence Stratigraphic Model

T1: Early Transgressive Systems Tract—Lower A-1 Carbonate

The onset of Lower A-1 Carbonate deposition is known to correspond to a third-order transgression following a sea-level lowstand associated with A-1 Evaporite deposition (Leibold, 1992). The observations presented herein generally agree with this interpretation. In the basin center Bruske core, the base of the Lower A-1 Carbonate directly overlies bedded halite of the A-1 Evaporite. Here, the Lower A-1 Carbonate consists of laminated microbial carbonate and anhydrite (Fig. 7) exhibiting high S and Sr values. Upward, these deposits gradationally transition vertically into a thin (15 cm) interval of stromatolitic rudstone. The lowermost A-1 Carbonate transgression is also associated with high GR values, as well as elevated Si, Al, and K concentrations, which are consistent with continued influx of continental windblown clastic material. The facies progression and geochemical signatures are interpreted to represent the first sea-level transgression associated with A-1 Carbonate deposition.

In the basin center, argillaceous carbonate laminites are observed immediately above the lowermost transgressive Lower A-1 Carbonate deposit. Here, the laminites persist vertically for the remainder of Lower A-1 Carbonate unit (Fig. 7). The transition from shallow-water, cyanobacterial mats to deep-water, pelagic laminites is interpreted to represent a rapid and sustained transgression through the Lower A-1 Carbonate. Pyritized surfaces associated with elevated concentrations of Fe and S (Fig. 7), indicative of deep-water reducing (redox) conditions, are also present throughout the basin center in the Lower A-1 Carbonate interval.

T2: Transgressive to Highstand Systems Tract—Lower A-1 Carbonate

The base of the Lower A-1 Carbonate, both in the northern reef flank position (Fig. 6) and the southern reef toe position (Fig. 5), shows elevated concentrations of continental proxy elements, similar to those observed in the basin center (Fig. 7). These are absent in the upper part of the Lower A-1 Carbonate, however. In the Kenney core (Fig. 6), for example, a very distinct shift from elevated continental proxy elements in the lower third of the Lower A-1 Carbonate to very low concentrations in the upper two thirds of the Lower A-1 Carbonate occurs around 6080 ft (1853 m). This shift also corresponds to lower GR values, as well as a lithofacies transition from the more argillaceous, thinly laminated mudstone in the lower third of the Lower A-1 Carbonate to the carbonate-rich, normally graded mudstone in the upper two thirds of the Lower A-1 Carbonate (Fig. 7). These observations reflect a shift in deposition during transgression at the base of Lower A-1 Carbonate to highstand deposition in the upper Lower A-1 Carbonate. A continued transgression would have effectively pushed the continental shoreline farther away from the basin center and increased carbonate production due to more oxygenated basin waters (lower Mo).

The presence of microbial lithofacies in the Lower A-1 Carbonate at the Columbus III reef flank position indicates that sea level reached the flanks of southern trend reef complexes during the first major transgression prior to Rabbit Ear Anhydrite deposition (T-2; Fig. 9). During Lower A-1 Carbonate transgression, however, there is no evidence that sea level reached the reef crest of southern reef complexes. This is supported further by the observation that deeper-water lithofacies, such as the normally graded mudstone and laminated peloidal wackestone, are absent in the reef flank position (Fig. 4A). The underlying Niagaran in the Columbus III reef flank core is 38 m thick, whereas in the reef crest position, it is ~115 m thick (Fig. 4A). If sea level had reached the reef crest position during Lower A-1 Carbonate transgression, the reef flank would have experienced water depths of >70 m, most likely resulting in the deposition of deeper-water facies. The only facies observed in the Lower A-1 Carbonate in the reef flank position below the Rabbit Ear Anhydrite is the stromatolitic rudstone, which we interpret to be a shallow-water deposit (Fig. 8A) based on vertical facies relationships.

The upper half of the Lower A-1 Carbonate in the northern shelf-slope reef flank position (Fig. 6) is composed of lithofacies indicative of deposition below storm wave base, as evidenced by the lack of wave-induced sedimentary structures, and the prevalence of graded turbidity deposits. The difference in sedimentation style observed in the northern C-21 reef flank position (deep water) compared to the southern Columbus III reef flank position (shallow water) suggests that peritidal conditions existed ~100 m farther updip on the northern reef complex during Lower A-1 Carbonate deposition than on the southern reef complex during the maximum extent of the transgression (T-2; Fig. 9). The observation that the Lower A-1 Carbonate in the northern shelf slope is ~3× thicker than the southern shelf slope (Fig. 10) supports an asymmetric basin rim height morphology, which controlled flooding of paleotopographic highs at different times (Fig. 10). This asymmetry could be a result of differential subsidence within the Michigan Basin, with the northern part of the basin undergoing greater rates of subsidence compared to the southern during this time. Differential subsidence was first proposed by Ells (1967), who noted taller, narrower reefs in the north compared to shorter and wider reefs in the south.

T3: Falling Stage to Lowstand Systems Tract—Rabbit Ear Anhydrite

Gradational facies transitions observed between the Lower A-1 Carbonate and the overlying Rabbit Ear Anhydrite indicate a shift from highstand conditions at end of Lower A-1 Carbonate deposition to falling sea level and subsequent basin restriction.

The lack of primary halite deposition in the Rabbit Ear Anhydrite suggests that basin waters never reached halite saturation during this regression. Thus, the magnitude of drawdown during Rabbit Ear Anhydrite deposition was not as dramatic as it was in the underlying A-1 Evaporite (third order), which is characterized by thick deposits of halite and sylvite (Fig. 10).

In the southern Columbus III reef complex (Fig. 4A), the first Rabbit Ear Anhydrite drawdown led to exposure of the reef flank position, resulting in paleosol formation (stromatolitic floatstone). The Rabbit Ear Anhydrite anhydrite fabrics observed in the Columbus III reef toe are separated by an inferred flooding and freshening event that led to deposition of the carbonate mudstone facies. A two-pronged shallowing is also observed in the basin center position (Fig. 7), where the lower Rabbit Ear Anhydrite is composed of slightly shallower-water thinly laminated mudstone (B_i). Although Rabbit Ear Anhydrite fabrics in this position were not observed during core description, elevated concentrations of S and Sr were clearly observed in association with facies B_i (Fig. 7).

The presence of anhydrite fabrics in the basin center position is proof that basin waters reached gypsum saturation during Rabbit Ear Anhydrite drawdown. The lack of sabkha-indicative fabrics in reef toe, interreef, and basin center positions, however, supports a model of subaqueous deposition for the nodular anhydrite mudstone facies of the Rabbit Ear Anhydrite. Further evidence for subaqueous gypsum sedimentation during the Rabbit Ear Anhydrite drawdown is that reef toe and basin center Rabbit Ear Anhydrite facies are bounded on either side by interpreted deep-water A-1 Carbonate facies (facies A and B). This contrasts with previous interpretations that Rabbit Ear Anhydrite fabrics formed solely in supratidal sabkha settings (Budros and Briggs, 1977; Gill, 1977). Facies relationships and geochemical signatures suggest that Rabbit Ear Anhydrite deposition in the basin center position was time-correlative with deposition observed in the shelf-slope environments. If the majority of the A-1 Carbonate facies observed in the basin center position were deposited in >100 m of water depth, our model allows for a time-correlative Rabbit Ear Anhydrite unit across the entire basin. If the basin center A-1 Carbonate facies were deposited in peritidal environments, as previously interpreted, then the entire Lower A-1 Carbonate, Rabbit Ear Anhydrite, and Upper A-1 Carbonate in the basin center position must have been deposited prior to deposition of the Lower A-1 Carbonate in the shelf-slope position. Identification of the Rabbit Ear Anhydrite in all basin positions, bounded by deep-water A-1 Carbonate facies, permits the new sequence stratigraphic interpretation to be made, and regional correlations of the entire A-1 Carbonate to be somewhat constrained chronostratigraphically.

T4: Transgressive to Highstand Systems Tract—Upper A-1 Carbonate

In all paleotopographic positions within the basin, the basal portion of the Upper A-1 Carbonate is characterized by deeper-water carbonate facies and higher concentrations of continental proxy elements (Figs. 5–7). These observations are consistent with a basinwide transgression that deposited the basal Upper A-1 Carbonate. In the basin center position (Fig. 7), a decrease in continental proxy elements at 7228 ft (2203 m) is interpreted to mark a transition from transgressive systems tract to highstand systems tract deposition. This transition is also evidenced by vertical facies assemblages indicative of a shallowing event and carbonate laminae that progressively thicken through the interval from millimeter to centimeter scale (Fig. 7). The presence of peritidal carbonate lithofacies in the reef crest position in all reef complexes examined here suggests that during Upper A-1 Carbonate transgression, sea level reached its maximum extent (T4; Fig. 9). A model of continued transgression through the Upper A-1 Carbonate is also supported by gradual decreases in continental proxy element concentrations throughout the interval.

CONCLUSIONS

Conventional core and gamma-ray log observations were integrated with elemental data from ED-XRF to identify 13 lithofacies in the A-1 Carbonate. Deposition of these lithofacies occurred at distinct paleotopographic positions within the Michigan Basin. In contrast to previous studies, which interpreted the A-1 Carbonate as a shallow peritidal deposit, the sedimentological and geochemical evidence presented here supports the idea that the A-1 Carbonate was deposited in a wide range of depositional environments and water depths. Of the 13 lithofacies identified in the A-1 Carbonate, six are consistent with deep-water deposition, including various anhydrite fabrics observed in the basin center position. Whereas shallow-water microbialites are associated with deposition at the reef crest and reef flank positions, the majority of depositional evidence at the reef flank, reef toe, shelf-slope interreef, and basin center positions reflects conditions below storm wave base. Sedimentary structures, such as scour surfaces at the bases of normally graded beds, and thin parallel laminations related to gravity-induced turbidity flows and distal pelagic deposition, are common.

A combination of core description and ED-XRF elemental signatures helped us to identify the Rabbit Ear Anhydrite unit in all paleotopographic positions throughout the Michigan Basin. Based on stacking patterns and stratigraphic relationships, the Rabbit Ear Anhydrite is interpreted to represent deposition during a time-correlative drawdown of sea level. This drawdown was marked by: (1) subaerial exposure and paleosol formation, (2) sabkha flats with associated deposition of enterolithic anhydrite, (3) subaqueous pelagic gypsum accumulation, (4) elevated concentrations of Si, Al, S, and Sr, which reflect terrigenous input, and (5) elevated concentrations of Mo and Ni associated with increased basin restriction.

Widespread deposition of the Rabbit Ear Anhydrite effectively bifurcates the A-1 Carbonate into an upper and lower unit. The stratigraphic position of the Rabbit Ear Anhydrite throughout the studied interval allowed a basinwide sequence stratigraphic model to be derived. Lower A-1 Carbonate deposits represent

a basinwide transgression, which corresponds to deep-water pelagic carbonate accumulation in the basin center and increased concentrations of Si, Al, and K interpreted to reflect increased influx of terrigenous material. The subsequent highstand deposits of the Lower A-1 Carbonate are marked by a decrease in continental proxy elements, coupled with a shallowing-upward succession of facies indicative of increased rates of carbonate production. Following basinwide regression and deposition of the Rabbit Ear Anhydrite, the Upper A-1 Carbonate represents a second major basinwide transgression, which culminated in deposition of shallow-water microbial facies atop Niagaran reef crests. Similar facies stacking and geochemical trends are observed in the Upper and Lower A-1 Carbonate units, with early transgressive deposits consisting of high concentrations of continental proxy elements, and lower concentrations in the subsequent highstand deposits.

Application of ED-XRF–derived elemental data in conjunction with observations from conventional tools such as core description and wireline logs allowed otherwise homogeneous carbonate lithofacies to be interrogated and interpreted more effectively. More specifically, elemental data can inform and improve core descriptions, and core descriptions provide valuable context for observed elemental trends. Finally, formation boundaries in sedimentary sequences can be further refined because shifts in elemental concentrations often predate observed changes in lithology. Both data sets are independently useful to study carbonate rocks, but they are far more powerful when integrated together.

ACKNOWLEDGMENTS

We would like to express our deepest gratitude to Linda and William Harrison III, and the staff at the Michigan Geological Repository for Research and Education (MGRRE), for providing all of the core and well data presented in this study. We would like to acknowledge Harry Rowe for making the mudrock calibration available, and for helpful suggestions. Bruce Kaiser also played an important role in X-ray fluorescence (XRF) data calibration and quantification. The technical contributions of Charlotte Sullivan are also appreciated. This work benefited from support and collaboration with Battelle Memorial as part of the Midwest Region Carbon Sequestration Partnership program, funded, in part, by the U.S. Department of Energy. Acquisition of XRF data was made possible through funding by National Science Foundation grant EAR-IF 1636441 awarded to Kaczmarek. This manuscript benefited from thorough reviews by Ron Budros and David Katz. We would also like to thank the editors of this volume, William Harrison III, David Barnes, and G. Michael Grammer, for constructive feedback and guidance.

REFERENCES CITED

Algeo, T., and Maynard, J., 2008, Trace-metal covariation as a guide to water-mass conditions in ancient anoxic marine environments: Geosphere, v. 4, no. 5, p. 872–887, doi:10.1130/GES00174.1.

Algeo, T., and Rowe, H., 2012, Paleoceanographic applications of trace-metal concentration data: Chemical Geology, v. 324–325, p. 6–18, doi:10.1016/j.chemgeo.2011.09.002.

Al Ibrahim, M.A.H., 2015, Multi-Scale Sequence Stratigraphy, Cyclostratigraphy, and Depositional Environment of Carbonate Mudrocks in the Tuwaiq Mountain and Hanifa Formations, Saudi Arabia [Master's thesis]: Golden, Colorado, Colorado School of Mines, 181 p.

Alling, H., and Briggs, L., 1961, Stratigraphy of Upper Silurian Cayugan evaporites: American Association of Petroleum Geologists Bulletin, v. 45, p. 515–547.

Banner, J., 1995, Application of trace element and isotope geochemistry of strontium to studies of carbonate diagenesis: Sedimentology, v. 42, p. 805–824, doi:10.1111/j.1365-3091.1995.tb00410.x.

Bhatia, M., and Cook, K., 1986, Trace element characteristics of graywackes and tectonic setting discrimination of sedimentary basins: Contributions to Mineralogy and Petrology, v. 92, p. 181–193, doi:10.1007/BF00375292.

Briggs, L., and Briggs, D., 1974, Niagara-Salina relationships in the Michigan Basin, *in* Kesling, R.V., ed., Silurian Reef-Evaporite Relationships: Lansing, Michigan, Michigan Basin Geological Society, Annual Field Conference Guidebook, p.1–23.

Briggs, L., Briggs, D., Elmore, D., and Gill, D., 1978, Stratigraphic facies of carbonate platform and basinal deposits, late middle Silurian, Michigan Basin, *in* Kesling, R.V., ed., The North-Central Section of the Geological Society of America Field Excursions: New York, Geological Society of America, p. 117–131.

Budros, R., 1974, The Stratigraphy and Petrogenesis of the Ruff Formation, Salina Group in Southeast Michigan [Master's thesis]: Ann Arbor, Michigan, University of Michigan, 178 p.

Budros, R., and Briggs, L., 1977, Depositional environment of Ruff Formation (Upper Silurian) in southeastern Michigan, *in* Fisher, J.H., ed., Reefs and Evaporites—Concepts and Depositional Models: American Association of Petroleum Geologists Studies in Geology 5, p. 53–71.

Catacosinos, P., Daniels, P., and Harrison, W., 1991, Structure, stratigraphy, and petroleum geology of the Michigan Basin, *in* Leighton, M.W., Kolata, D.R., Oltz, D.T., and Eidel, J.J., eds., Interior Cratonic Basins: American Association of Petroleum Geologists Memoir 51, p. 561–601.

Droste, J., and Shaver, R., 1985, Comparative stratigraphic framework for Silurian reefs; Michigan Basin to surrounding platforms, *in* Cercone, K.R., and Budai, J.M., eds., Ordovician and Silurian Rock of the Michigan Basin and Its Margins: Michigan Basin Geological Society Special Paper 4, p. 73–93.

Ells, G., 1967, Information on Michigan's Silurian Oil and Gas Pools: Lansing, Michigan, Department of Conservation, Michigan Geological Survey Division, 34 p.

Feldmann, M., and McKenzie, J., 1997, Messinian stromatolite-thrombolite associations, Santa Pola, SE Spain: An analogue for the Paleozoic: Sedimentology, v. 44, p. 893–914, doi:10.1046/j.1365-3091.1997.d01-53.x.

Friedman, G., and Kopaska-Merkel, D., 1991, Late Silurian Pinnacle Reefs of the Michigan Basin, *in* Catacosinos, P., and Daniels, P., Jr., eds., Early Sedimentary Evolution of the Michigan Basin: Geological Society of America Special Paper 256, p. 89–100, doi:10.1130/SPE256-p89.

Garber, R., Levy, Y., and Friedman, G., 1987, The sedimentology of the Dead Sea: Carbonates and Evaporites, v. 2, p. 43–57, doi:10.1007/BF03174303.

Gardner, W., and Bray, E., 1984, Oils and source rocks of Niagaran reefs (Silurian) in the Michigan basin, *in* Palacas, J.C., ed., Petroleum Geochemistry and Source Rock Potential of Carbonate Rocks: American Association of Petroleum Geologists Studies in Geology 18, p. 33–44.

Gill, D., 1973, Stratigraphy, Facies, Evolution and Diagenesis of Productive Niagaran Guelph Reefs and Cayugan Sabkha Deposits, the Bell River Mills Gas Field, Michigan Basin [Ph.D. diss.]: Ann Arbor, Michigan, University of Michigan, 275 p.

Gill, D., 1977, Salina A-1 sabkha cycles and the Late Silurian paleogeography of the Michigan Basin: Journal of Sedimentary Petrology, v. 47, no. 3, p. 979–1017.

Gill, D., 1985, Depositional facies of Middle Silurian (Niagaran) pinnacle reefs, Belle River Mills gas field, Michigan Basin, southeastern Michigan, *in* Roehl, P.O., and Choquette, P.W., eds., Carbonate Petroleum Reservoirs: New York, Springer-Verlag, p. 121–139, doi:10.1007/978-1-4612-5040-1_8.

Grammer, M., Barnes, D., Harrison, B., III, Sandomierski, A., and Mannes, R., 2009, Practical synergies for increasing domestic oil production and geological sequestration of anthropogenic CO_2: An example from

the Michigan Basin, *in* Grobe, M., Pashin, J.C., and Dodge, R.L., eds., Carbon Dioxide Sequestration in Geological Media—State of Science: American Association of Petroleum Geologists Studies in Geology 59, p. 689–706.

Haug, G., Riedermann, R., Zahn, R., and Ravelo, C., 2001, Role of Panama uplift on oceanic freshwater balance: Geology, v. 29, no. 3, p. 207–210, doi:10.1130/0091-7613(2001)029<0207:ROPUOO>2.0.CO;2.

Huh, J., 1973, Geology and Diagenesis of the Niagaran Pinnacle Reefs in the Northern Shelf of the Michigan Basin [Ph.D. diss.]: Ann Arbor, Michigan, University of Michigan, 253 p.

Jodry, R., 1969, Growth and dolomitization of Silurian reefs, St. Clair County, Michigan: American Association of Petroleum Geologists Bulletin, v. 53, no. 4, p. 957–981.

Kujau, A., Nuernberg, D., Zielhofer, C., Bahr, A., and Roehl, U., 2010, Mississippi River discharge over the last approximately 560,000 years; indications from X-ray fluorescence core-scanning: Palaeogeography, Palaeoclimatology, Palaeoecology, v. 298, no. 3–4, p. 311–318, doi:10.1016/j.palaeo.2010.10.005.

Leibold, A., 1992, Sedimentological and Geochemical Constraints on Niagara/Salina Deposition, Michigan Basin [Ph.D. diss.]: Ann Arbor, Michigan, University of Michigan, 280 p.

Mantek, W., 1973, Niagaran pinnacle reefs in Michigan, *in* Ontario Petroleum Institute, 12th Annual Conference, London, Ontario, p. 35–46.

Mesolella, K., Robinson, J., McCormick, L., and Ormiston, A., 1974, Cyclic deposition of Silurian carbonates and evaporites in the Michigan Basin: American Association of Petroleum Geologists Bulletin, v. 58, no. 1, p. 34–62.

Michigan Department of Environmental Quality, 2015, Annual Report: Michigan Office of Oil, Gas, and Minerals, Oil and Gas Miner database, http://www.michigan.gov/deq (accessed 1 April 2017).

Nurmi, R., 1975, Stratigraphy and Sedimentology of the Lower Salina Group (Upper Silurian) in the Michigan Basin [Ph.D. dissertation]: Troy, New York, Rensselaer Polytechnic Institute, 261.

Nurmi, R., and Friedman, G., 1977, Sedimentology and depositional environments of basin-center evaporites, Lower Salina Group (Upper Silurian), Michigan Basin, *in* Fisher, J.H., ed., Reefs and Evaporites—Concepts and Depositional Models: American Association of Petroleum Geologists Studies in Geology 5, p. 23–52.

Obermajer, M., Fowler, M., Snowdon, L., and Macqueen, R., 2000, Compositional variability of crude oils and source kerogen in the Silurian carbonate-evaporite sequences of the eastern Michigan Basin, Ontario, Canada: Bulletin of Canadian Petroleum Geology, v. 48, no. 4, p. 307–322, doi:10.2113/48.4.307.

Pearce, T., and Jarvis, I., 1992, Applications of geochemical data to modelling sediment dispersal patterns in distal turbidites: Late Quaternary of the Madeira abyssal plain: Journal of Sedimentary Petrology, v. 62, p. 1112–1129.

Pearce, T., Besly, B., Wray, D., and Wright, D., 1999, Chemostratigraphy: A method to improve interwell correlation in barren sequences—A case study using onshore Duckmantian/Stephanian sequences (West Midlands, UK): Sedimentary Geology, v. 124, p. 197–220, doi:10.1016/S0037-0738(98)00128-6.

Pierce, J., and Parker, J., 2015, Identifying landing zones utilizing high-resolution x-ray fluorescence (XRF) chemostratigraphy, *in* Blasingame, T., Rhodes, S., and Sparkman, G., chairpersons, Proceedings of the 3rd Unconventional Resources Technology Conference: San Antonio, Texas, Society of Exploration Geophysicists, p. 1–8.

Playton, T., Jansen, X., and Kerans, C., 2010, Carbonate slopes, *in* Dalrymple, R., and James, N., eds., Facies Models 4: St. John's, Newfoundland, Geological Association of Canada, p. 449–476.

Riding, R., 2011, Microbialites, stromatolites, and thrombolites, *in* Reitner, J., and Thiel, V., eds., Encyclopedia of Geobiology: Dordrecht, Netherlands, Springer, p. 635–654, doi:10.1007/978-1-4020-9212-1_196.

Rimmer, S., 2004, Geochemical paleoredox indicators in Devonian-Mississippian black shales, Central Appalachian Basin; USA: Chemical Geology, v. 206, no. 3–4, p. 373–391, doi:10.1016/j.chemgeo.2003.12.029.

Rine, M., Garrett, J., and Kaczmarek, S.E., 2017, A new facies architecture model for the Silurian Niagara–Lower Salina "pinnacle" reef complexes of the Michigan Basin, *in* MacNeil, A., Lonnee, J., and Wood, R., eds., Advances in Characterization and Modeling of Complex Carbonate Reservoirs—In Memory of Eric Mountjoy: Society of Sedimentary Geology (SEPM) Special Publication 109, doi:10.2110/sepmsp.109.02.

Ritter, A., and Grammer, G.M., 2017, this volume, Utilizing sequence stratigraphy to develop a depositional model for Silurian (Niagaran) reefs in the Michigan Basin, *in* Grammer, G.M., Harrison, W.B., III, and Barnes, D.A., eds., Paleozoic Stratigraphy and Resources of the Michigan Basin: Geological Society of America Special Paper 531, doi:10.1130/2017.2531(05).

Rowe, H., Hughes, N., and Robinson, K., 2012, The quantification and application of handheld energy-dispersive X-ray fluorescence (ED-XRF) in mudrock chemostratigraphy and geochemistry: Chemical Geology, v. 324–325, p. 122–131, doi:10.1016/j.chemgeo.2011.12.023.

Sageman, B., and Lyons, T., 2004, Geochemistry of fine-grained sediments and sedimentary rocks, *in* Mackenzie, F., ed., Sediments, Diagenesis, and Sedimentary Rock: Treatise on Geochemistry, Volume 7: Amsterdam, Netherlands, Elsevier, p. 115–158.

Sarg, J., 1982, Off-reef salina deposition (Silurian), southern Michigan Basin: Implications for reef genesis, *in* Handford, C.R., ed., Depositional and Diagenetic Spectra of Evaporites, Calgary: Society of Sedimentary Geology (SEPM) Core Workshop, v. 3, p. 354–384.

Scotese, C., 2002, PALEOMAP Website: http://www.scotese.com (accessed 1 April 2017).

Sears, S., and Lucia, F., 1979, Reef-growth model for Silurian pinnacle reefs, northern Michigan reef trend: Geology, v. 7, p. 299–302, doi:10.1130/0091-7613(1979)7<299:RMFSPR>2.0.CO;2.

Tjallingii, R., Roehl, U., Koelling, M., and Bickert, T., 2007, Influence of the water content on X-ray fluorescence core-scanning measurements in soft marine sediments: Geochemistry Geophysics Geosystems, v. 8, no. 2, Q02004, doi:10.1029/2006GC001393.

Tribovillard, N., Algeo, T., Lyons, T., and Riboullleau, A., 2006, Trace elements as paleoredox and paleoproductivity proxies: An update: Chemical Geology, v. 232, p. 12–32, doi:10.1016/j.chemgeo.2006.02.012.

Turner, B., Treanton, J., and Slatt, R., 2016, The use of chemostratigraphy to refine ambiguous sequence stratigraphic correlations in marine mudrocks. An example from the Woodford Shale, Oklahoma, USA: Journal of the Geological Society, London, v. 173, p. 854–868, doi:10.1144/jgs2015-125.

Warren, J., 2016, Evaporites: A Geological Compendium (2nd ed.): Berlin, Springer International Publishing, 1813 p.

Wold, J.L., and Grammer, G.M., 2017, this volume, Rock-based 3-D reservoir characterization of a Silurian (Niagaran) reef—Ray gas storage field, Macomb County, Michigan, *in* Grammer, G.M., Harrison, W.B., III, and Barnes, D.A., eds., Paleozoic Stratigraphy and Resources of the Michigan Basin: Geological Society of America Special Paper 531, doi:10.1130/2017.2531(06).

Wu, T., and Boak, J., 2015, Chemostratigraphic analysis of Green River Formation in Douglas Pass, Piceance Basin: A response to the depositional environment, *in* Blasingame, T., Rhodes, S., and Sparkman, G., chairpersons, Unconventional Resources Technology Conference: San Antonio, Texas, Society of Exploration Geophysicists, p. 290–401.

Manuscript Accepted by the Society 9 June 2017
Manuscript Published Online 9 November 2017